Universidad
de La Laguna

Trabajo fin de grado
2018-2019

The Rossiter-McLaughlin effect in exoplanets

Tutors:
Núria Casasayas Barris
Enric Pallé Bagó

Author:
Mar Rivera Colomer

Contents

Abstract

Historically, one of the burning questions of astronomy deals with the exoplanet's topic, in other words the search of any planet beyond the Solar System. In this project we introduce a first theoretical chapter in which the definition of exoplanet is stipulated, the main detection techniques described and a brief analysis of the instruments used. The aim of this study is studying the Rossiter-McLaughlin (RM) effect in WASP-69b using CARMENES data. The RM is an anomaly of the RV due the blockage of part of the host star's light. It can be detected with high-resolution spectrographs, such as HARPS and CARMENES, that are enough accurate to detect the Doppler shifts in the spectrum of the star caused by the planet's motion. The RM effect can be used to study and characterise the atmosphere of exoplanets, although it is difficult to resolve the spectral lines stems from high stellar activity and telluric contamination from the terrestrial atmosphere.

We will observe how the telluric contamination and the stellar activity alter the RV data and the RM parameters. To do this, we will use a pipeline called SERVAL, removing the highly contaminated regions to compare if this has an improvement on the results. The data used are from two transit observations of WASP-69b with the CARMENES spectrograph, located at the Calar Alto observatory. In addition, we will measure the chromatic RM effect of WASP-69b following the method described by DiGloria et al. (2015).

In the results we can observe that the errors are clearly reduced when we exclude the contaminated orders, as expected. However, for the chromatic RM effect the errors are too large to conclude something precise. To yield good results, and get accurate atmospheric properties, more transits are needed as well as high resolution observations with larger telescopes.

Acknowledgement

1 Introduction

1.1 What is an exoplanet?

In the resolution B5 (IAU, 2006) was established the definition of a planet. A planet is a celestial body that:

(a) Is in orbit around the Sun.

(b) Has sufficient mass for itself-gravity to overcome rigid body forces so that it assumes a hydrostatic equilibrium (nearly round) shape.

(c) Has cleared the neighbourhood around its orbit.

In the IAU 2003 recommendation an exoplanet or extrasolar planet is defined as a planet which orbits a star outside (beyond) the Solar System. This generic definition includes the following objects:

1. Objects with true mass below the limiting mass for thermonuclear fusion of deuterium that orbit star or stellar remnants are planets (no matter how they formed). This mass is currently calculated to be $13M_J$ for objects of solar metallicity. The minimum mass required for an exoplanet is the same used in the Solar System, and it is $3.7x10^{19}$ kg.

2. Substellar objects with true masses above the limiting mass for thermonuclear fusion of deuterium are brown dwarfs.

3. Free-floating objects in young star clusters with masses below the limiting mass for thermonuclear fusion of deuterium are not planet, but sub-brown dwarfs.

The question about the existence of other worlds in the cosmos is an ancient question, at least it dates back to the Ancient Greek. To have today's interpretation, so that the words *search for other worlds* correspond to the search for exoplanets, two fundamental astronomical discoveries have been necessary. The first one is the heliocentric system established by Nicolaus Copernicus in the book *De revolutionibus* published in 1543, and the second discovery is the understanding that stars are other suns, an idea from Giordano Bruno that comes up at the end of s.XVI.

The discovery of the first exoplanet took place in the 1900s thanks to the analysis of periodic Doppler shifts in stellar spectra. Since the first confirmation of an exoplanet, thousands of them have been found, a lot of investigation have been carried out, and new horizons are continually being opened. A recent statistical estimation places, on average, at least one planet around every star in the galaxy. In particular, the first exoplanet was discovered in the 1992 by Aleksander Wolszczan and Dale Frail. It was a rocky planet orbiting a pulsar in the Virgo constellation, but the real step on this field was on 1995 with the discovery of the first exoplanet around a main sequence (MS) star. The discovery was made by Didier Queloz and Michel Mayor using the radial velocity method in the specific star 51 Pegasi. In the following years, with the development of other detection methods, the discovery of new different kinds of exoplanets experienced an exponential rise.

In 2001, the team lead by David Charbonneau and Timothy Brown did the first measurement of an extrasolar planet's atmosphere. They used the space-based spectrometer on board the Hubble Space Telescope (HST) to analyze the atmospheric composition. Their study revealed the presence of atomic sodium (NaI) on the HD 209458b's atmosphere. This doublet is one of the easiest species to detect in a hot planet upper atmosphere due to its high cross-section, and the line cores can trace the temperature profiles up to the planet thermosphere. Since then, the atmospheric characterization of some of these

discovered planets has been rapidly expanding with the constantly improvement of the astrophysical instrumentation, being the transiting systems the most amenable targets for atmospheric studies.

The first rocky terrestrial planet was announced in February 2009 and it was discovered by CoRoT, a French-led ESA satellite. It was not until 2015 that the first near-Earth sized candidate, Kepler-452b, orbiting a solar candidate in the habitable zone was announced. It was discovered by the famous mission Kepler space telescope that began observing potential terrestrial planets in the habitable zone in 2011.

Exoplanets have presented an uninterrupted stream of unexpected surprises and are being discovered each year in data from surveys around a wide variety of stellar types, ranging from MS to low-mass stars, giant stars, and other advanced evolutionary stages such as white dwarfs and pulsars. Consequently, the evolution of these planets have been different, resulting in a very large diversity from isolated hot-Jupiters on retrograde orbits to tightly-packed, multi-planet systems of super-Earths. However, still none seem to quite resemble the Earth nor to be arranged in a structure similar to that of our Solar System. In Figure 1 we show a polar plot with a representation of 2510 out of 4095 confirmed exoplanets from the *Exoplanet.eu database* until 26 June 2019. When writing this memory, there are around 3600 discovered planets (considering the NASA Exoplanet Archive, till 1 January 2018).
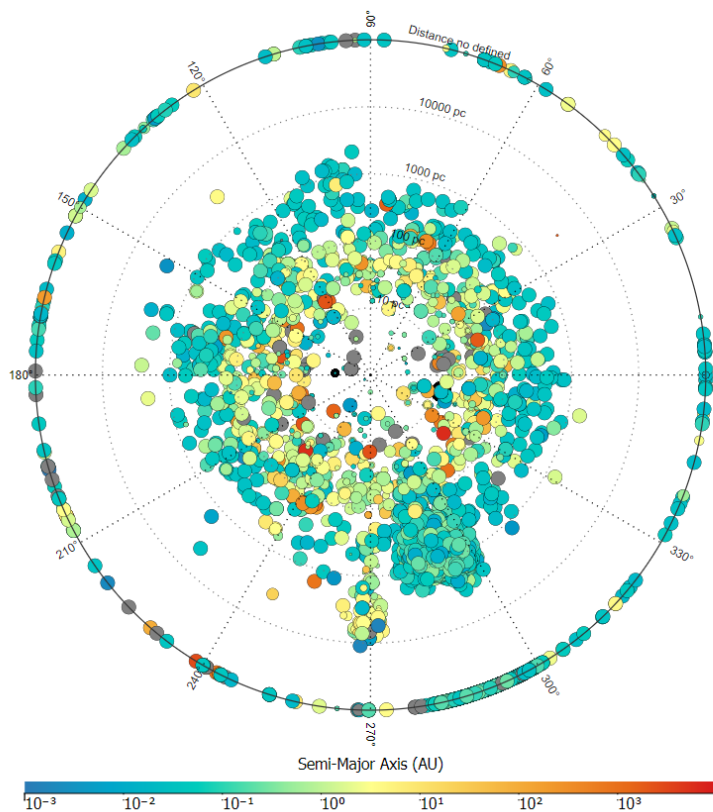

Figure 1: Exoplanet's polar plot, depending on the semi-major axis (in AU). Extracted from *http://exoplanet.eu*.

1.2 Detection methods

The first discovery of an exoplanet was carried out by observing small periodic variations of stellar radial velocities. During some years, this was the unique successful method, but nowadays one of the most efficient ones is the detection of transits. Most of the detection methods were indirect, due to the weak luminosity of the planets and the proximity with their host star, so the methods were based on the effects that the planet(s) produce on the star. Recently, some studies are making emphasis in direct detection methods. In the Figure 2 we can see a summarized sketch of the exoplanet detection methods and the number of exoplanets discovered using each of them.

The discovery of an exoplanet begins with the observation of a sign in a star through any method, then we talk about possible candidate. Subsequently, the candidate is thoroughly studied by means of a combination of various methods in order to dismiss other causes that can provoke similar effects on the star. Terrestrial exoplanets have so far been detected primary via the microlensing method, though they now are being discovered by the transit and radial velocity techniques.

In this chapter we summarise the main areas of exoplanet research, combining a description of detecting methods and important physical concepts. We strongly focus on the transit and radial-velocity methods, which are the ones used in this work.
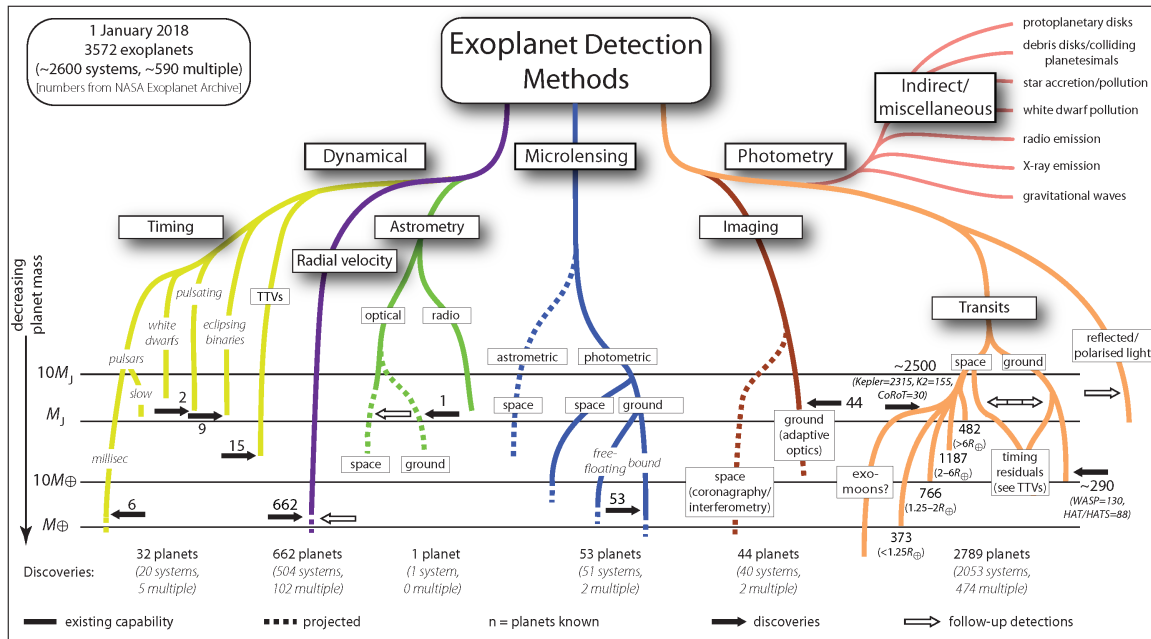
Figure 2: Perryman tree: display of the different methods, organized into a hierarchy. Extracted from NASA exoplanet archive, a service of NASA exoplanet Science Institute.

1.2.1 Transits method

It consists in photmetrically observe the star and detect subtle changes on the apparent magnitude when the planet is orbiting around. In other words, the observation of the periodical decreasing of the luminosity of the star due to the presence of planets between the star and the observer.

In the beginnings, this method was used to investigate the Solar System planets. The observation of Mercury's transit carried out by Pierre Gassendi in 1631 was the first observation of a planet

transiting in front of the Sun. Detecting transits with photometry observations has arguably been the most successful exoplanet discovery method to date. The boost of this method was thanks to Kepler's mission, a space telescope launched by NASA on 2009 with the aim to discover Earth-size planets orbiting other stars. The acceptance of the method is the fact that planets discovered by transits across bright host stars permit the extraction of a wealth of information form further observations. So we can say, succinctly, that the method strength is the rich set of parameters that can be characterized form the transiting planets (in particular in combination with radial velocity observations) as period, diameter, mass and chemical atmospheric composition. But it also have drawbacks, which are the low probability that transits appears in randomly oriented planet system and the false positives stems from other astrophysical phenomena. The intense work to provide the community with efficient transit fitting routines to extract the most useful set of physical parameters from transit light curves has made possible that, nowadays, more than a half of the several thousands of exoplanets were discovered by the transit method.

The method only works for star-planet systems that have orbits aligned in such a way that, as seen form the Earth, the planet travels between us and the star and temporally blocks some of the light from the star once every orbit. A planet usually only blocks the 1% of the light or less. The method has a bias towards discovering large planets orbiting close to their stars, because larger planets block more light and transit more frequently so they are easier to detect.

First of all, it is necessary to introduce some basic concepts, which can be easily understood through Figure 3. An *eclipse* is the (partial) obscuration of one celestial body by another. The term *transit* refers to the movement of the smaller object (in our study: the exoplanets) in front of the host star, at the time of inferior conjunction. We will talk about *occultation or secondary transit* to refer to the planet passing behind the star (superior conjunction). The star of the transit is marked by the *first contact* that it is when the projected outer rim of the planet makes contact with the projected outer rim of the star, and similarly for fourth contact on exit. Second and third contact are the times when the projected planet lies just inside the projected rim of the star, on ingress and egress, as can be observed in Figure 4.
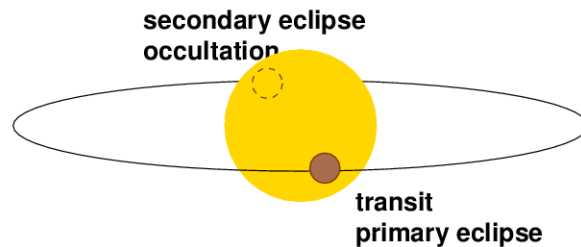
Figure 3: Schematic view of a primary and secondary eclipses. Extracted from *http://spiff.rit.edu*.

When a planet passes directly between the observer and the star that it is orbiting, the star's light dims by a measurable amount. This measurable level of light being observed from the star is drawn in a chart called light curve. When the planet passes in front of the star and blocks some of its light, the light curve indicates this drop in brightness. The size and lengths of a transit can tell a lot about the planet that's causing the transit. The amount of time between each transit tells us about the planet's orbit and radii. Densities can be obtained form their masses, which give us a first estimate of their composition or internal structure. Applying photometry and spectroscopy methods during

the different transit, allow us to characterise the exoplanet's atmosphere because some of the starlight passes through its atmosphere.

If we now focus on the equations, we can say that during the transit the planet blocks, progressively, a fraction of the star light, so the star's flux diminishes by a fractional denoted as ΔF. After the transit, the planet's brighter day-side progressively comes into view, and the total flux raises and it drops again during the secondary eclipse as the planet passes behind the star. This process is described schematically on Figure 4. Under the assumptions of negligible flux from the planet and of spherical shapes of the star and planet, ΔF is given by the ratio of the areas of the planet and the star:

$$\Delta F \approx \left(\frac{R_p}{R_s}\right)^2 = k^2 \tag{1}$$

where R_p is the radius of the planet, R_s the radius of the star and k is the radius ratio (R_p/R_s). The total transit duration t_T is between first and fourth contact. The time of totality, in which the entire planet disk is in front of the stellar disk or during which the light curve is relatively flat (the time between second and third contacts) is given by t_F.
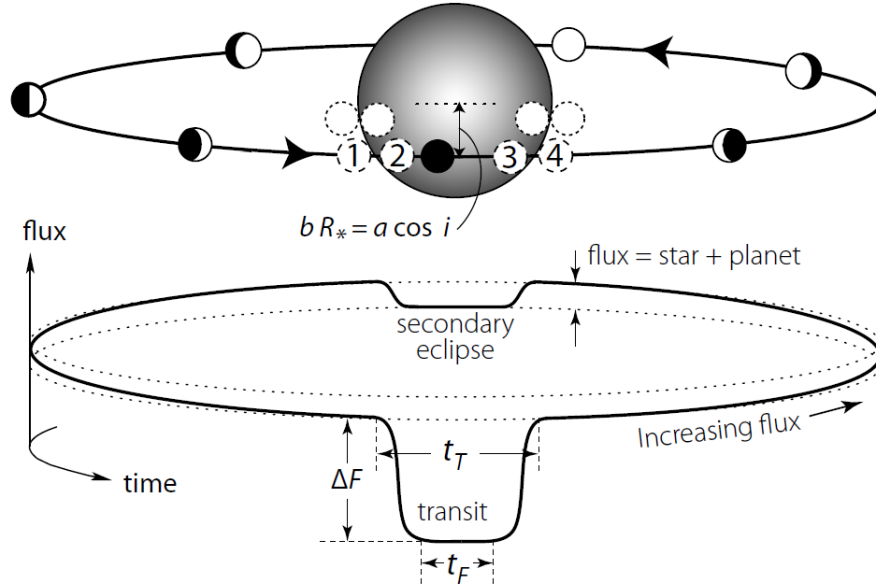
Figure 4: Scheme of a transit. Dashed circles show the first to fourth contact points. Extracted from Winn et al. (2009).

The impact parameter b is defined as the minimal projected distance to the center of the stellar disk during the transit, and it can be expressed as:

$$b \equiv \frac{a}{R_s}\cos i = \left[\frac{(1-k)^2 - \left[\sin^2(t_F\pi/P)/\sin^2(t_T\pi/P)\right](1+k)^2}{\cos^2(t_F\pi/P)/\cos^2(t_T\pi/P)}\right]^{1/2} \tag{2}$$

where a is the orbital semi major axis, i is the orbital inclination, and P the period.

The (geometric) probability for a random-oriented planet to be favourably aligned for a transit is given by:

$$p = \left(\frac{R_s \pm R_p}{a}\right)\left(\frac{1 + e\sin\omega}{1 - e^2}\right) \tag{3}$$

where e is the eccentricity of the orbit. The $+$ sign is used to include grazing transits and the $-$ sign refers to the full transits that have second and third contacts. For a typical Hot Jupiter with a semi major axis of 0.05 AU, this probability is of the order of 10%, while for an Earth-like planet at 1 AU from a solar-like star, it goes down to 0.5%. Consequently, the majority of existing planet systems will not display transits, this is the main handicap of the method.

The construction of theoretical transit light curves, are used to obtain properties of the transiting planet-star systems. It follows a quite simple idea: one projected sphere (that of the planet) passes across another (the star) and the light form the star is attenuated according to the fraction of the two surfaces which overlap. The complications appear when we include other effects like: stellar limb darkening, light reflected from the planet, blending due to background objects and the effects due to orbit eccentricity. Limb darkening refers to the drop of intensity in a stellar image moving from the center to its limb, and results from the combined effects of optical depth with the decreasing star density and temperature with radius. The effect is very significant for planetary transits, giving rise to a small colour change with wavelength, although it diminishes with increasing wavelengths.

Nearby exoplanet host stars are typically comparatively bright, and telescope apertures can be very large. For surveys of the brightest stars, the contribution of photon noise to photometric transit measurements is generally negligible. On the other hand, limitations on the smallest transit depths ΔF, and hence the smallest planet masses, arise from a combination of atmospheric transparency variations, atmospheric scintillation noise, and detector granularity. Very stable sites in terms of atmospheric transparency fluctuations are required before scintillation dominates. Ground-based telescopes are presently able to discover exoplanet transits with depths up to about $(\Delta F/F) \simeq 1\%$.

1.2.2 Radial velocities method

Most of what we know about heavens comes from information encoded in various forms of light, so certain properties of stars and celestial bodies are easily to determinate than others. For example, the position on the sky and the motion of objects in the plane of the sky can be measured with great accuracy thanks to the Doppler shift. Here, we will introduce the spectroscopic technique, which is also called the method of radial velocities (shortened in RV), which measure the radial component (along the line of sight) of the velocity of the star. We will focus on the measurements, including the different instrumental approaches being used and under development. It was the technique through which the first exoplanets were discovered and it's based on the observation of small Doppler shifts in the spectrum of a star. These shifts are due to the motion of the star around the star-planet barycenter (center of mass) due to the orbiting planets. This wobble in the space, that causes change of the color of light, is not directly visible at the telescope but whose presence can be inferred thanks to its gravitational pull on its parent star, see Figure 5. We can use the redshift of the objects to know if they are moving towards us (blue displacement, shorter wavelengths) or farther away (redshift).
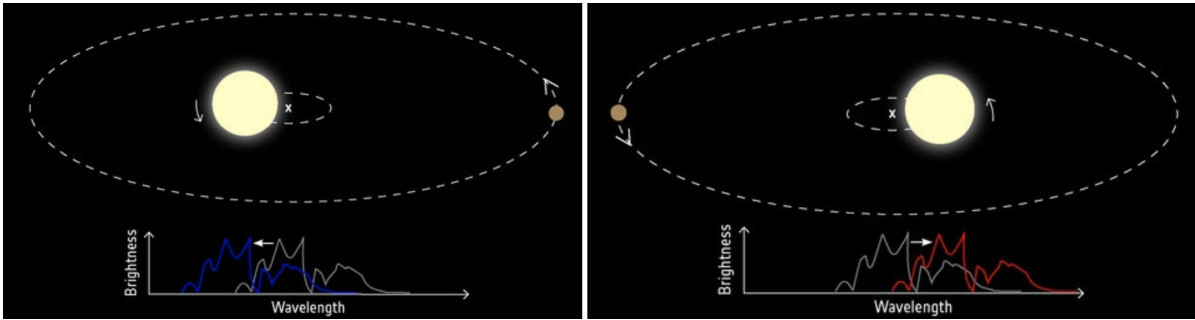
Figure 5: Sketch of the RV change of the stellar spectrum due to the presence of a planet orbiting around. Extracted from *http://sci.esa.int/gaia*, and self-adapted.

In all binary systems, the objects (host star and exoplanet/s) orbit the common system barycentre. The motion is described with an elliptical orbit, described in the Figure 6, with the center of mass on the focus. The orbits of the system can be described by seven parameters: a, e, P, t_p, i, Ω and ω. Where the semi-major axis a of the orbiting body with respect to the system barycentre and the eccentricity e specify the size and shape of the elliptical orbit. P is the period and it's related through Kepler's third law of the planetary motion: $P^2 = \frac{4\pi^2}{GM}a^3$. t_p corresponds to the position of the object along its orbit at a particular reference time. The remaining parameters are angles and represent the projection of the true orbit into the apparent (observed) one: i is the orbit inclination with respect to the reference plane (the particular case $i=0$ corresponds to a face-on orbit), Ω is the longitude of the ascending node (it's the node where the measured object moves away from the observer through the plane of reference) and ω is the argument of the pericenter being the angular coordinate of the object's pericenter. The pericenter (q) and the apocenter (Q) distances are given by: q= $a(1-e)$ and Q= $a(1+e)$.
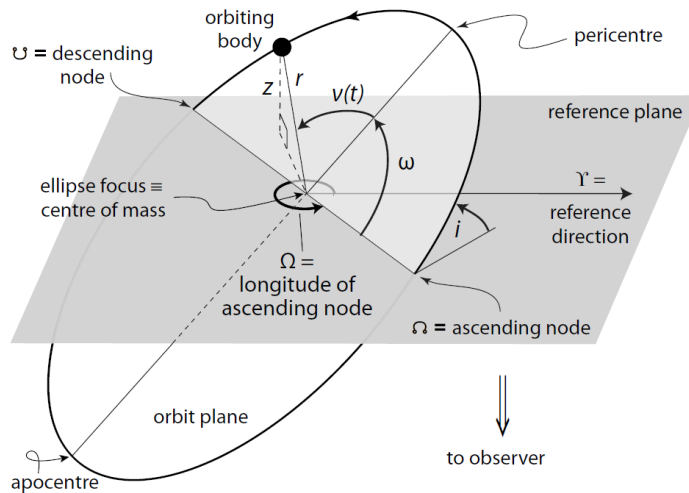
Figure 6: Elliptical orbit in three dimensions. The reference plane is tangent to the celestial sphere. Extracted from *The Exoplanet handbook* (figure 2.2), Perryman, M.

Binary systems can provide important information about their structure. The relative masses of the host star and exoplanet can be measured with their orbits and their common center of mass. From the ratio of the RV's amplitudes along the line-of-sight we can describe the semi-amplitude of the RV variations K over the course of an orbit:

$$K \equiv \frac{2\pi}{P} \frac{a_s \sin i}{(1 - e^2)^{1/2}} \qquad ; \qquad K^2 = \frac{G}{(1 - e^2)} \frac{1}{a_s \sin i} \frac{M_p^3 \sin^3 i}{(M_s + M_p)^2} \tag{4}$$

To relate the properties of the system we will use the *mass function, f*:

$$f \equiv \frac{PK^3(1 - e^2)^{\frac{3}{2}}}{2\pi G} = \frac{M_{\text{unseen}}^3 \sin^3 i}{(M_{\text{unseen}} + M_{\text{seen}})^2} \tag{5}$$

where G is Newton's constant.

The phase and orientation of the elliptical orbit with respect to the line of sight are represented by the parameter T_0 and ω, and the overall radial velocity of center of mass is usually given by γ. The orbital parameters measured represent the orbit of the observed star with respect the system's center of mass. In single-lined system, the existence of the unseen object (exoplanet) is often deduced from this motion, and its orbital parameters are identical except that K is scaled by a factor of M_{unseen}/M_{seen} and ω differs by π. This application of RV is highly used to detect extrasolar planets from some years ago. When we study exoplanets we can approximate the mass function in the large mass-ratio limit:

$$\frac{M_{unseen}}{M_{seen}} = \frac{M_{planet}}{M_{star}} \ll 1 \tag{6}$$

yielding the more familiar equation relating the amplitude of a Doppler shift to the mass and orbital properties of the planet:

$$K \approx \left(\frac{2\pi G}{P M_s^2} \right)^{\frac{1}{3}} \frac{M_p \sin i}{\sqrt{1 - e^2}} \tag{7}$$

For the RV measurements of a single exoplanet system, the best fitting solution is a sinusoidal that represent the RV depending on time, as we can see in Figure 7.
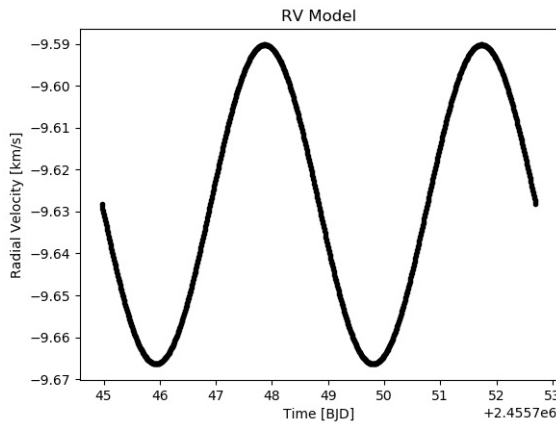
Figure 7: RV change produced by a particular planet orbiting a particular star modelled using SinRadVel from PyAstronomy Library.

The detection with precise RVs depends on the planet's mass, the inclination, and the orbital period (there is also a dependence on orbital eccentricity, which is complex but insignificant for low eccentricities). The period dependence is weak, and for giant planets, the detection is often limited more by the duration of the observations than their RV amplitude. To scale, we can also express the quantities in the following units:

$$K = 0.64 \; m/s \cdot (1 - e^2)^{-1/2} \left(\frac{P}{days} \right)^{1/3} \left(\frac{M_*}{M_\odot} \right)^{-2/3} \frac{M_p}{M_{Earth}} \sin i \tag{8}$$

With this final expression is easier to see that the dependence on stellar mass means that exoplanet detection is in principle most sensitive around the lowest mass star. An instantaneous measurement of the stellar RV about the star-planet barycenter is given by the small systematic Doppler shift in wavelength of the many absorption lines that make up the star's spectrum. The Doppler formula that allows us to calculate the relative radial speed between the star and the observatory that measured the light v_r via the redshift z is the following:

$$z \equiv \frac{\lambda_{obs} - \lambda_{rest}}{\lambda_{rest}} = \frac{1}{\gamma(1 + v_r/c)} - 1 \tag{9}$$

where γ is the relativistic factor, c the speed of light and v the scalar relative speed between the frame of the star and the observatory.

Such measurements have accuracy limited by the wavelength calibration of the spectrograph and understanding of complicated factors such as the internal motions of the emitting material and redshifts from general relativity. High-accuracy RVs for exoplanet detection are typically acquired using Echelle spectrographs with high spectral resolving power (typically $R = 50000 - 100000$), and operated in the optical region (450-700 nm). The high resolution spectrographs (HRS) are necessary to measure precisely the small red- and blueshift of the host star's spectrum as it moves towards and way form us in response to the gravitational pull of its exoplanet throughout its orbit.

1.2.3   Echelle spectrographs generalities

The spectroscopy is the study of the interaction between matter and electromagnetic radiation. And the spectrograph is a device used to measure properties of light over a specific portion of the electromagnetic spectrum. This instrument separates light by its wavelengths with a diffraction grating and record the data. There are different types of dispersion, we will focus on high dispersion Echelle spectrographs.

Echelle means ladder in french, hence the connotation here where the spectral orders correspond to the rungs of the ladder as a result of the dispersion in the vertical and horizontal directions (orthogonal directions). An Echelle spectrograph uses two dispersion stages so it has two dispersive elements. As a result, the spectral data is displayed as a 2D pattern and can be ideally captured with a 2D detector (like a CCD). To get a high resolution dispersion and less polarization effects, it uses a plane grating at high angles of incidence, and the diffraction grating with low density of lines. This characteristics offer an extraordinary resolution on very high orders. The overlap of the spectra is severe, so it is necessary to introduce the second dispersive element to separate the different orders. This introduces a deformation of the spectra that must be corrected by further image processing. The Echelle spectrograph scheme can be seen in Figure 8. The high resolution Echelle spectrographs currently working on exoplanets search and characterization projects are those seen in the Figure 9. Their main characteristics are described in Table 1.
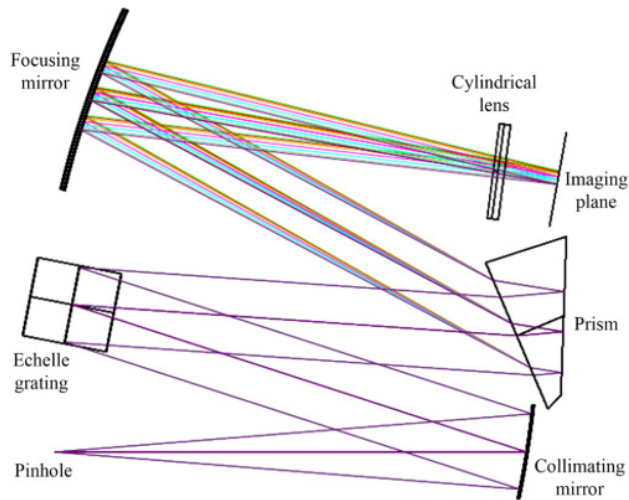
Figure 8: Sketch of an Echelle spectrograph. Extracted from *Astigmatism-corrected Echelle spectrometer using an off-the-shelf cylindrical lens*, Xiao Fu et al. (2017).
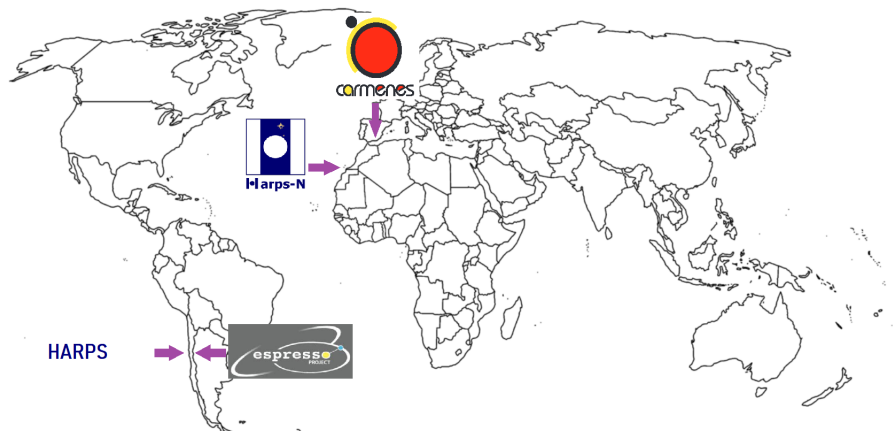
Figure 9: Location of the main Echelle spectrographs used for exoplanetary studies.

Parameters	Espresso	HARPS-N	HARPS	CARMENES
Location	Paranal (Chile)	La Palma (Spain)	La Silla (Chile)	Calar Alto (Spain)
Telescope	VLT (8m)	TNG (3.58m)	ESO (3.6m)	No-named (3.5m)
Scope	Rocky planets	Terrestrial planets	?	M dwarfs with exoplanets
Resolution, R	~200 000	115 000	115 000	~90 000
λ coverage (nm)	380-686	383-693	378-691	visible: 520-960 N-IR: 960-1710
λ precision	5 m/s	0.97 m/s	0.97 m/s	1m/s
RV stability	<10 cm/s	<30 cm/s	<30 cm/s	

Table 1: Main characteristics of the Echelle spectrographs.

High instrumental stability and accurate wavelengths calibration is demanded to minimise effects of gravitational and thermal telescope flexures, and other instrument drifts. Large telescopes and long integration times are still required to achieve the necessary high signal-to-noise, and corresponding sub-pixel accuracy. In Figure 10 we show the evolution of the precision achieved by these HRS.
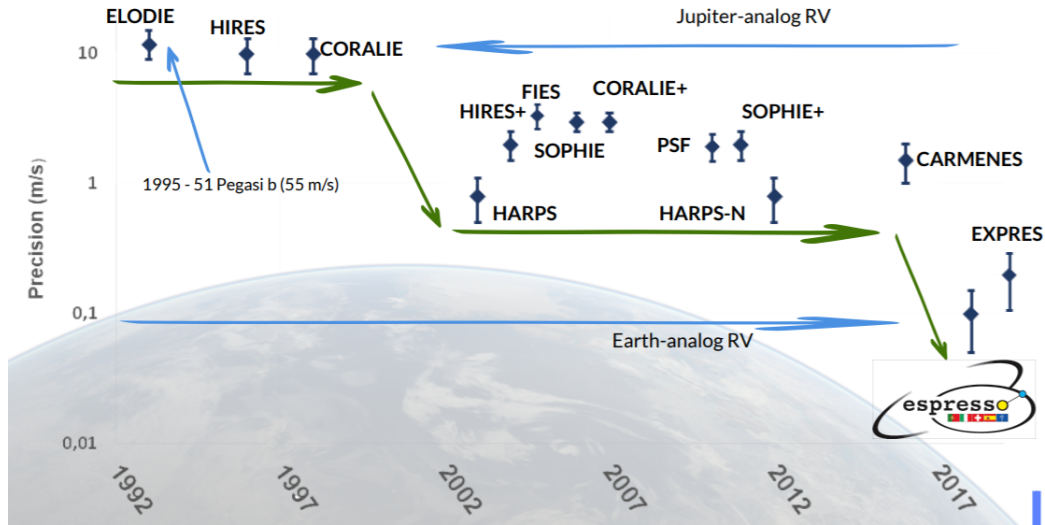
Figure 10: Evolution of the precision reached by different spectrographs. Extracted from Mascareño, A. presentation (2019).

These methods will be crucial in the near-future in order to detect very small planets, and characterize spectral features of rocky planets and super-Earths atmospheres, which will be out of reach of the James Webb Space Telescope (JWST), but available with facilities such as ESPRESSO on the Very Large Telescope (VLT).

1.2.4 Cross-correlation techniques

In signal processing, as we can see in the Figure 11, cross-correlation is a measure of similarity of two series as a function of the displacement of one relative to the other. In our case, for RV measurements, we will have the observed spectrum and, in the other hand, a theoretical mask.
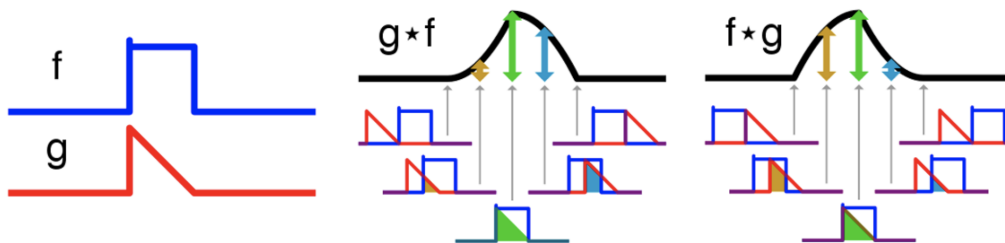
Figure 11: Cross-correlation method. Extracted from Wikipedia (*https://en.wikipedia.org/*) and self-adapted.

Cross-correlation spectroscopy consists in finding the information about the instantaneous Doppler shift, which is combined in many thousands of absorption lines, present in the high-resolution optical spectrum of stars. This information can be concentrated into a few parameters by cross-correlation, even at low signal-to-noise levels. Limitations remain in fixing the physical template, in accuracy and adaptability to spectral type. The precise shape of the resulting cross-correlation depends on the intrinsic spectral lines shapes and on the template line widths, representing a mean profile of all lines in the template.

RV surveys tend to focus on inactive stars because of the inherent difficulty in determining whether the source of an RV signal in stellar activity or reflex motion induced by an orbiting body. Transit surveys are not affected by this ambiguity, as stellar activity does not produce transit-like features in light curves. The separation of the RV contributions due to reflex motion from those due to activity can be simple or unnecessary in case of short period, giant transiting planets, but it is non-trivial for lower mass planets.

1.2.5   Other methods

Direct imaging: Before the discovery of the first exoplanet astronomers have been seeking to detect these celestial bodies using imaging methods. Nonetheless direct imaging is still in its beginning stages as an exoplanet-finding method, but there are high expectation that it will be a good tool, because it might be able to take photos that allow us to identify atmospheric patterns, oceans and landmasses. Nowadays no more than 40 planets have been discovered with this technique. One of the most famous example of direct imaging is the following Figure 12.
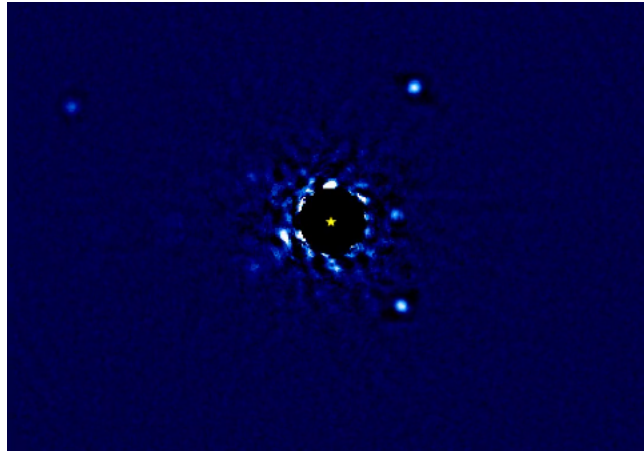
Figure 12: Example of direct imaging. Four planets more massive than Jupiter orbiting the young star HR 8799. It is a composition of images taken during 7 years at the W.M. Keck observatory in Hawaii. Extracted from Astrobiology at NASA (*https://astrobiology.nasa.gov/*).

The main problem is that the stars are millions of times brighter than their planets. Any light reflected off the planet (infrared radiation) or heat radiation from the planet itself is drowned out by a massive amounts of radiation coming from its host star. So it is most effective in the infrared where the contrast ratio is favourable. For imaging substellar companions using ground-based telescope modern extreme adaptive optics (Ex-AO) and various techniques to block out the light are necessary. Using these instruments it is possible to detect planets down to a few M_{Jup} in the 10-30 AU range. Once the

glare of the star is reduced, they can get a better look at objects around the star. The main methods to block the light of stars that might have planets orbiting them are:

- Coronography: uses a device inside a telescope to block light from a star before it reaches the telescope's detector. Now are being used from the ground-based observatories

- Starshade: a device that's positioned to block the light from a star before it even enters a telescope. They are used in spacecrafts.

*Gravitational microlensing*: This effect causes the distortion of the light which changes direction when affected by the gravity of massive object. In general relativity, the presence of matter distorts space-time and, as a result, the path of electromagnetic radiation is deflected. When from our viewpoint one star passes in front of another star, light rays from a distant background object are bent by gravitational potential of a foreground object (the lens) to create images of the source which are distorted and which may be highly focused and hence significantly amplified. In the microlensing regime discrete images of the source are unresolved at typical telescope resolutions. The exoplanet system acts as a multiple lens, and a more distant star within the Galaxy acts as the probing source. The changing magnification of the sub-images due to the time-varying alignment geometry let a significant intensity variation. Monitoring the light curve as the alignment changes over several hours allows the additional lensing effects of an accompanying planet to be identify. At least 80 planets have been discovered by this method, most of all are Jupiter-analogs. The principle advantage is that this method is sensitive to multiple planet system and free-floating planets. In the diagram of the Figure 13 an undetected planet is shown orbiting a star. The image of the background star becomes distorted by the gravitational field of the foreground star, which acts like a lens focusing light towards the observer on Earth. If a planet is near the focused light it contributes to the lensing effect, and can be detected on Earth as a disturbance to the light being received from the distant star
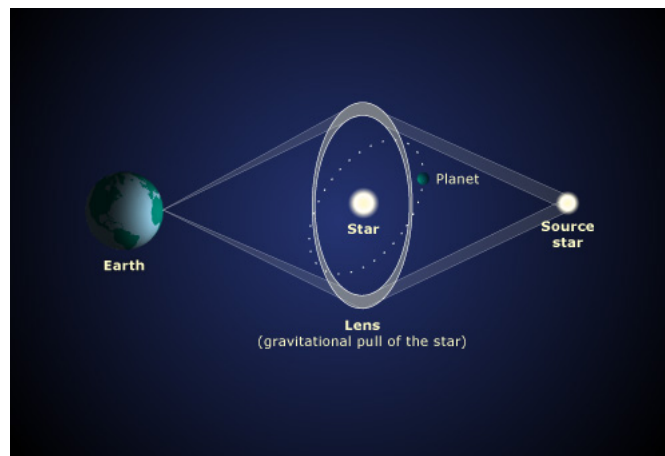
Figure 13: Sketch of gravitational microlensing. Extracted form *https://teara.govt.nz/en.*

Astrometry: The history of astrometry is linked to the history of star catalogues, which gave astronomers reference points for objects in the sky so they could track their movements, the stellar parallaxes and the proper motion. This method concerns the measurement of positions and motions of celestial bodies within the galaxy. Doppler shift are not the only way astronomers can find stars that are wobbling due to the gravity of their planets. The wobble can also be visible as changes in

the star's apparent position in the sky, as seen on the Figure 14. It's a hard method, as stars wobble around one minute distance, being very difficult to accurately detect it, especially for small ones. The technique consist on taking series of images of these stars containing planets and some of the other stars that are near them in the sky. In each picture, the distances between these reference stars and the star with possible planets are compared. The aim of high-accuracy astrometry is to determine the transverse component of the displacement of the host star due the gravitational perturbation of an orbiting planet and it can also be used to determine the mass of the extrasolar planets. The manifestation of the gravitational influence is related to the corresponding photocentre displacement along the line-of-sight and it more sensitive to planets with large orbits. Astrometry is more accurate in space missions that are not affected by the distorting effects of the Earth's atmosphere. One example is the European Space Agency's Gaia Mission, launched in 2013 that applies astrometric techniques in its stellar census. Nowadays only one planet has been discovered within this detection method.
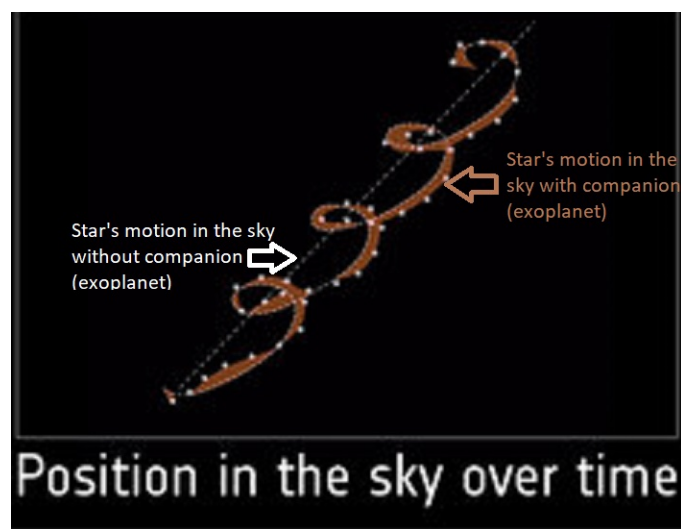
Figure 14: Sketch of astrometry. Extracted from *http://sci.esa.int/gaia* and self-modified.

Timing: An orbiting planet is accompanied by a periodic oscillation of the position of the host star around the system barycentre, recognisable through changes in the RV and astrometric position of the primary. If the primary also possesses periodic times signatures, then these can provide an alternative route to the dynamical detection of orbiting planets through the change of the light travel time (measurement of orbit timing residuals). This has an amplitude related to the displacement of the primary along the line-of-sight. There are three cases of object, in addition to transiting planets, which offer this possibility: radio pulsars, pulsating stars and eclipsing binaries. The summarized performance of the method is described in Figure 15.

Before the optical discovery of exoplanets, radio pulsar timing techniques provided the first evidence for extra solar planets. It is a method with extraordinary precision. Pulsars emit intense electromagnetic radiation that is detected on Earth as regular and precisely timed pulses. Slight regular variations in the timing of the pulses indicate that the pulsar is moving back and forth, orbiting the center of mass of a system with one or more planets. This method allows to deduce the orbit as well as the mass of theses planets by precisely measuring irregularities in the timing of the pulsars. Although this is one of the most sensitive methods, the number of pulsars with orbiting planetary bodies has remained surprisingly small with no more than 30 exoplanets discovered using this method.
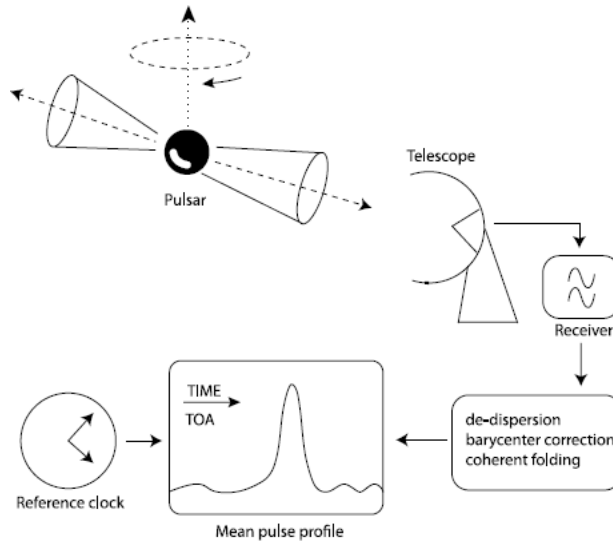
Figure 15: Sketch of pulsar timing. Extracted from the article *Pulsar Timing and Its Application for Navigation and Gravitational Wave Detection*, Werner Becker et al. (2018).

1.3 The Rossiter-McLaughlin effect

1.3.1 Theory

The Rossiter-McLaughlin (RM) effect appears as an anomalous RV variation happening over the Doppler reflex motion that an orbiting planet imparts on its rotating host star, and consequently blocking surface elements with different Doppler shifts at different times. This produces a distortion of the stellar spectral lines during the transit. The shape of the RM provides information about the ratio of the sizes between the planet and its host star, the rotational speed of the star, the impact parameter and the angle called λ, which is the sky-projected spin-orbit angle. It is an important element in the orbital characterization of transiting exoplanets, specially for formation and evolution theories.

In 1893, J. R. Holt proposed a method to measure the stellar rotation of stars using RV measurements, and he predicted that when one star of an eclipsing binary eclipsed the other it would first cover the advancing blueshifted half and then the receding redshifted half. But the effect takes its name from a pair of studies published jointly by R. A. Rossiter and D. B. McLaughlin on 1924, which interpret that this effect should be visible during exoplanetary transits as a small positive or negative anomaly in the RV curve, caused by the progressive occultation of the rotating stellar disk. The first reported RM effect for an exoplanet was on the 2000 by D. Queloz in the case of HD 209458b.

A rotating star has one of its hemispheres blue shifted and its other hemisphere red shifted. This happens because one of its sides is approaching to the observer while the other recedes. During a transit, part of the rotating stellar surface is hidden sequentially, weakening the corresponding velocity components of the stellar absorption lines. For instance, it can start covering the blue-shifted side (approaching), in this case the average flux received by the observer will appear red-shifted, creating a positive shift in the RV measured of the star, deviating from the Doppler reflex motion. An illustration of how this effect affects the spectral lines can be observed in Figure 16.
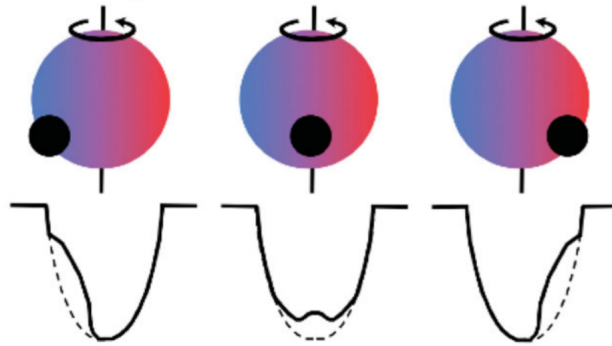
Figure 16: Sketch of the RM effect in the spectral lines depending on the orbital position of the planet. Extracted from Collier Cameron et al. (2010).

The maximum amplitude of the anomaly is called the semi-amplitude of the RM effect and it scales with the planet's size and the stellar rotational velocity:

$$A_{RM} \simeq \frac{2}{3} D v \sin i_\star \sqrt{1 - b^2} \tag{10}$$

where $D = (R_p/R_s)^2$ is the transit depth, R the radius, v the rotational velocity of the star (at the equator), $\sin i_\star$ is the inclination on the sky of the stellar rotation axis and b the impact parameter.

The shape of the RM effect contains several pieces of information. As we can see in the Figure 17 the light curve obtained with the RM effect depends on the geometry of the system.
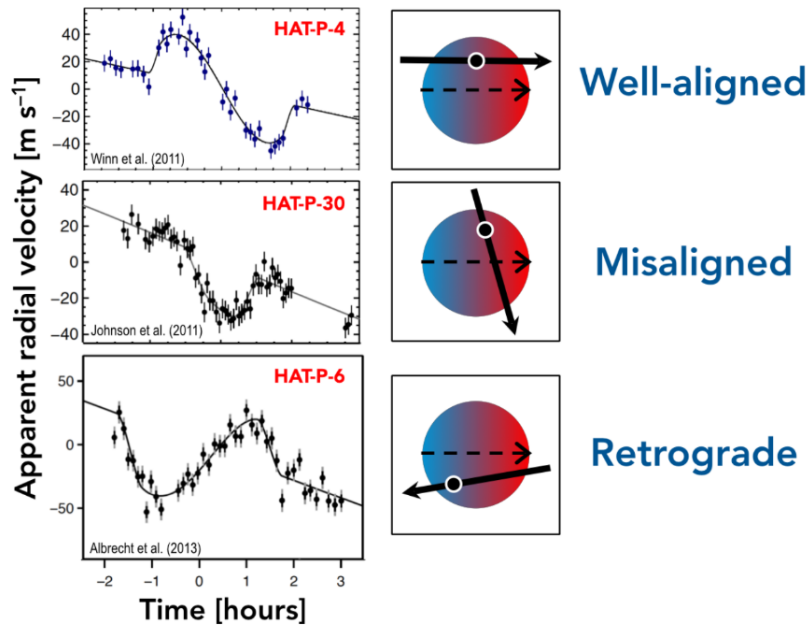
Figure 17: The RM effect of different exoplanets. Left: corresponding RV signals. Right: three transit geometries that produce identical photometric light curves, but differ in spin-orbit alignment. Extracted from the Princeton University web page (*https://web.astro.princeton.edu/files/orbitspng*).

The distribution of the λ values with other planetary or stellar parameters can be used to study the exchange of angular momentum between the planet and its host star, via tidal forces. And also it could be used to measure the orbital inclination of eclipsing binary stars and the rotational spin direction of exoplanets. Additionally, the effect is, as well, used in atmospheric investigations, because the opacity source within a planetary atmosphere (atoms, molecules, particles) lead to a variation in apparent size of the planet, which is observed as a variation of the transit depth, as a function of wavelength.

The RM signal can be detected when collecting high-cadence RV measurements made with high-precision, stable, high-resolution spectrographs such as those routinely used in the search for exoplanets. Nowadays, the effect can be used to confirm that an object is a planet, when RV precision is sufficient to rule out companion stars and brown dwarfs but too poor to enable the measurement of planetary mass. So accurate modeling of the RM effect are thus needed to get reliable information on the current obliquity of stars and to test theoretical predictions. To measure the RM effec,t RV measurements are performed during transits as we explained in section 1.2.2 and then compared with models to find the parameters that define the curve.

1.3.2   Chromatic RM

In 2004 Snellen et al. proposed an interesting suggestion, which was to use the RM effect as diagnostic of the atmosphere of a transiting planet. As observed in Equation (10), the overall amplitude of the RM effect (A_{RM}) depends on the effective size of the planet. Subsequently, the amplitude of the RM effect is also wavelength dependent and can be measured if we have high precision RV measurements.

The advantage of this method over conventional transmission spectroscopy measurements is that instead of using the intensity of on-transit spectra as a reference for in-transit spectra, it depends on the changes in the profiles of the stellar spectral lines in the same on-transit spectra. For ground-based observation this makes the technique less likely to be influenced by Earth atmospheric effects, which turned out to be challenging for the conventional approach, because line shapes are less influenced by telluric absorption.

In the same way that we could measure RM with all the spectra, we can also do it for different orders (colors). With this we are able to get RV measurements in different regions of the spectrum and finally can compare the results at different wavelengths. The chromatic RM effect gives us information about the Rayleigh scattering slope in the transmission spectrum with the aim to show that it can be effectively used to measure broadband transmission features.

The Rayleigh scattering is defined as predominantly elastic scattering of light or electromagnetic radiation by particles much smaller than the wavelength of the radiation. The Rayleigh scattering cross-section can be written as

$$\sigma = \sigma_0 \left(\lambda/\lambda_0\right)^{\alpha} \tag{11}$$

where α=-4 and therefore the slope of the planet radius as a function of wavelength is given by $\frac{dR_P}{d ln\lambda} = \frac{\mu g}{k}\alpha T$, where μ is the mean mass of the atmospheric particles, taken as 2.3 times the mass of the proton, k is the Boltzamann constant, and g the surface gravity.

In the Figure 18 we can see a simple sketch of the Rayleigh scattering effect. We observe that if the sky has a clear, upward-extended, hydrogen-dominated atmosphere, Rayleigh scattering disperses a large portion of the blue light from the atmosphere of the host, while it scatters less portion of the red light. As a result, a transit in blue light becomes deeper than the one in red light range (top). In the middle panel we can see a less extended, water-rich atmosphere, in this case the Rayleigh scattering's effect is much weaker, so the transits in all wavelength range have the same transit depths. The bottom panel shows that if the sky has extended clouds, most of the light cannot be transmitted through the atmosphere, so the transit depths will be almost the same even though hydrogen dominates.
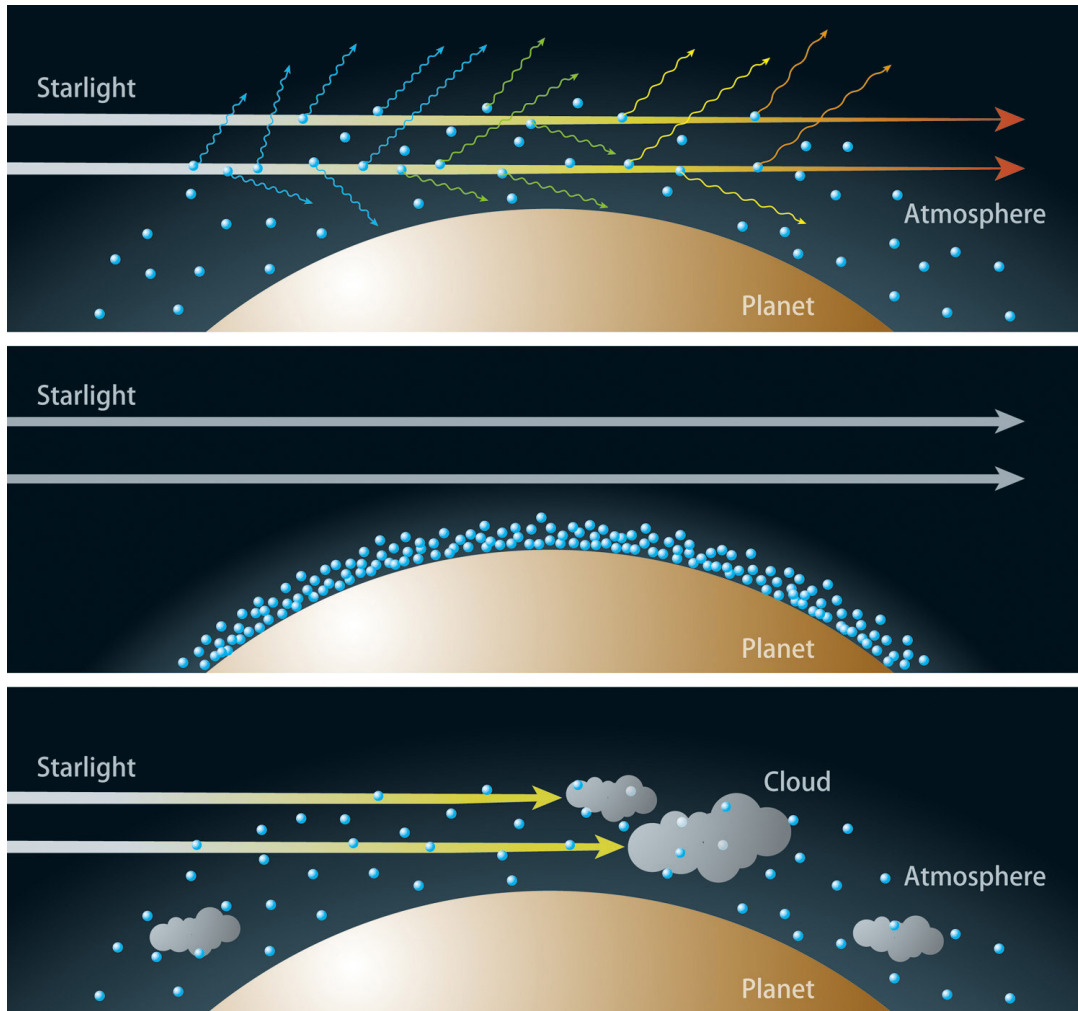
Figure 18: Sketch of the Rayleigh scattering in different cases. Extracted from NASA Exoplanet exploration web page (*https://exoplanets.nasa.gov/*).

The measurement of the Rayleigh scattering using the chromatic RM effect has been previously studied on HD 189733b by DiGloria et al. (2015) and Pont et al. (2013). The motivation of the study was that these measurements only depend on the differences in the profiles of the stellar spectral lines in same on-transit spectra and that it is less likely to be influenced by systematic effects. They used HARPS archival data, and they cover wavelengths from 378 nm to 691 nm over 72 orders.

DiGloria et al. (2015) interpreted that the optical transmission spectrum of HD 189733b presents Rayleigh scattering. From the slope of the fit in R_p/R_s ratio as a function of the natural logarithm of the wavelength, an estimation of the atmospheric temperature (at pressures where the scattering takes place) can be derived. The results obtained can be seen on Figure 19. However, in other literature like in McCullough et al. (2014) it has been advocated that star spots or plages might also result in the observed slope in the transmission spectrum. So the study actually notes that chromatic RM effect as used to determine the effective planet radius as function of wavelength is affected by star spots and/or plages.

This method will be particularly interesting in conjunction with the new Echelle spectrograph ESPRESSO, at Very Large Telescope, and will provide a gain in signal-to-noise ratio of about a factor 4 compared to HARPS, covering a larger wavelength regime.
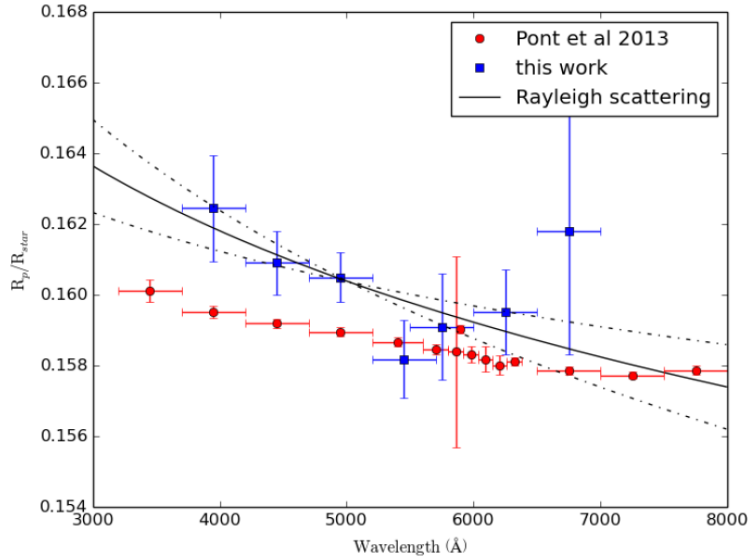
Figure 19: Results and comparison of the measurements of R_p/R_s from DiGloria et al. (2015) (blue) and Pont et al. (2013) (red). The solid line indicates the least-squares fit of Rayleigh-scattering slope. Extracted from DiGloria et al. (2015).

Rayleigh scattering has also been observed in different exoplanets, as those presented in Sing et al. (2016). They focus on the case of possibles clouds in different hot-Jupiter exoplanets. They observed eight transiting hot-Jupiters with the Hubble Space Telescope (HST) in the full optical wavelength range (0.3-1.01 μm). The resulting transmission spectra are shown in Figure 20 and exhibit a variety of spectral absorption features due to the presence of Na, K and H_2O, as well as strong optical scattering slopes. However, the amplitude of the H_2O absorption varies significantly across the planets, for example we can see that WASP-12b's slope is almost a flat line without peaks, due to the presence of clouds in the atmosphere that don't allow the light to be transmitted. In comparison we have WASP-17b, for which the Rayleigh scattering slope can be clearly seen.
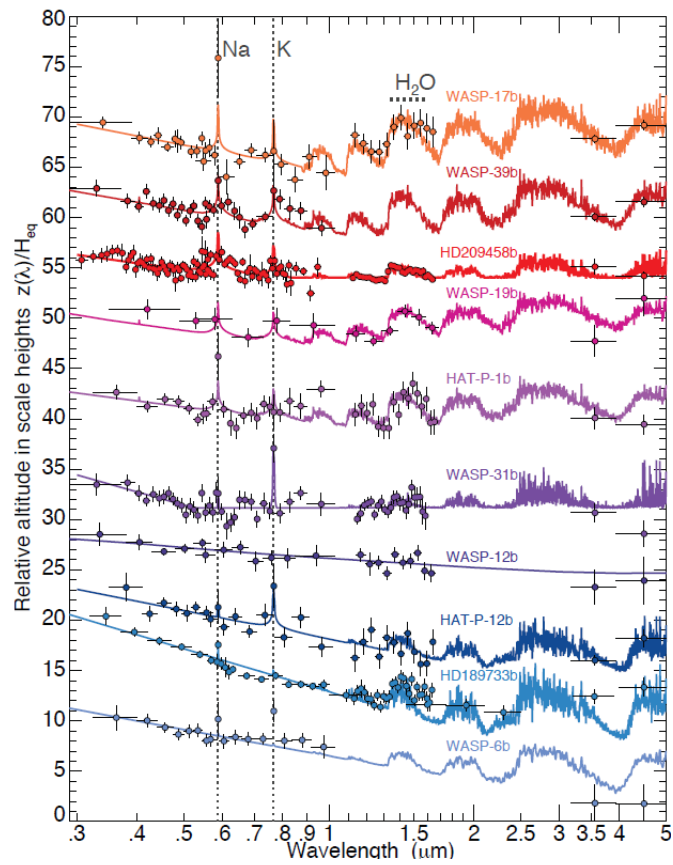
Figure 20: Transmission spectral sequence of hot-Jupiter survey targets. Extracted from Sing et al. (2016).

2 Goals

There are many methods of detecting exoplanets, being transit and radial-velocity methods two of the most important ones. If we combine both methods, which means measuring the radial-velocity change of the star when a planet is transiting in front of it, we can measure a radial-velocity anomaly called Rossiter-McLaughlin (RM) effect. The RM effect allows us to obtain some parameters of the system and, if we observe its evolution in wavelength, that can also be used to study and characterise the atmosphere of particular exoplanets by measuring the Rayleigh scattering slope. This project studies this RM effect for the exoplanet WASP-69b using CARMENES observations. The aim of this work is to observe how the telluric contamination and the stellar activity alter the RV data and the RM parameters. To do this, we will use an existing pipeline called SERVAL, removing the highly contaminated regions to compare if this has an improvement on the results. Additionally, we will try to measure the chromatic RM effect following the method introduced by DiGloria et al. (2015).

3   The target: WASP-69b

WASP-69b is a bloated Saturn-mass planet with mass of $0.26 M_{Jup}$ (with R_p=1.057 R$_J$) that orbits an active mid-K dwarf (K5 star) in 3.868 days.The system is composed by a giant planet and a bright host star (with magnitude V∼9.87). It is located approximately 50 pc away, and the semi-major axis is a=0.045 AU. The physical and orbital parameters of the target are presented in Figure 21.

Parameter	Symbol (unit)	WASP-69b
Orbital period	P (d)	$3.868\,1382 \pm 0.000\,0017$
Epoch of mid-transit	T_c (BJD, UTC)	$2455748.83344 \pm 0.00018$
Transit duration	T_{14} (d)	0.0929 ± 0.0012
Transit ingress/egress duration	$T_{12} = T_{34}$ (d)	0.0192 ± 0.0014
Planet-to-star area ratio	$\Delta F = R_p^2/R_*^2$	$0.017\,86 \pm 0.000\,42$
Impact parameter	b	0.686 ± 0.023
Orbital inclination	i (°)	86.71 ± 0.20
Stellar reflex velocity semi-amplitude	K_1 (m s^{-1})	38.1 ± 2.4
Systemic velocity	γ (m s^{-1})	$-9\,628.26 \pm 0.23$
Offset between CORALIE and HARPS	$\Delta\gamma_{\text{HARPS}}$ (m s^{-1})	—
Eccentricity	e	0 (adopted) ($<$0.10 at 2σ)
Stellar mass	M_* (M$_\odot$)	0.826 ± 0.029
Stellar radius	R_* (R$_\odot$)	0.813 ± 0.028
Stellar surface gravity	$\log g_*$ (cgs)	4.535 ± 0.023
Stellar density	ρ_* ($\rho_\odot$)	1.54 ± 0.13
Stellar effective temperature	T_{eff} (K)	4715 ± 50
Stellar metallicity	[Fe/H]	0.144 ± 0.077
Planetary mass	M_P (M_{Jup})	0.260 ± 0.017
Planetary radius	R_P (R_{Jup})	1.057 ± 0.047
Planetary surface gravity	$\log g_P$ (cgs)	2.726 ± 0.046
Planetary density	ρ_P (ρ_J)	0.219 ± 0.031
Orbital major semi-axis	a (au)	$0.045\,25 \pm 0.000\,53$
Planetary equilibrium temperature	T_{eql} (K)	963 ± 18

Figure 21: Parameters of the planet and star of the system. Extracted from the discovery paper Anderson et al. (2014).

Periodic dimming in the WASP (Wide Angle Search for Planets) light curves of WASP-69b were detected, and Anderson et al. (2014) identified the exoplanet as a candidate, based on data from the candidate selection process described in Collier Cameron et al. (2007). It was considered a possible candidate. The spectra of the host star were obtained using the CORALIE spectrograph mounted on the Euler-Swiss 1.2m telescope. RV measurements were computed by weighted cross-correlation with a K5-spectral template. RV variations were detected with periods similar to those found from the WASP photometry and with semi-amplitudes consistent with planetary-mass companions.

They tested the hypothesis that the RV variations are due to spectral-lines distortions caused by a blended eclipsing binary or star-spots by performing a line-bisector analysis of the cross-correlation functions. But the lack of correlation supports the conclusion that the periodic dimming and RV variation of each system are instead caused by a transiting planet. To prove the existence a total of 6

full/partial transits were observed during the following two seasons (2009-2010).

So the exoplanet was confirmed in 2011 using the transit method with the ground-based photometric survey WASP, which monitors bright stars (V=8-15) using two eight-camera arrays, each one with a field of view of 450 deg^2. There are two stations, WASP-South is hosted by the South African Astronomical Observatory and the SuperWASP-North station which is hosted by the Isaac Newton Group in the Observatorio Roque de Los Muchachos (La Palma). It is currently the ground-based search that has detected the major number of planets that stand out for their suitability for deeper characterization work, due to their short orbital period and/or large size.

There is no significant detection of lithium in the spectra of WASP-69, implying an age of at least 0.5 Gyr. It is a low-density planet in a short orbit around a relatively-young active star, so could be undergoing significant mass-loss due to X-ray-driven or extreme-ultraviolet-driven evaporation, the mass-loss rate is very high and of the magnitude order $\sim 10^{12}$ gs^{-1}. As we can see in Figure 22 the exoplanet WASP-69b drags a comet-like tail formed by helium particles escaping from its gravitational field propelled by the ultraviolet radiation from its star.
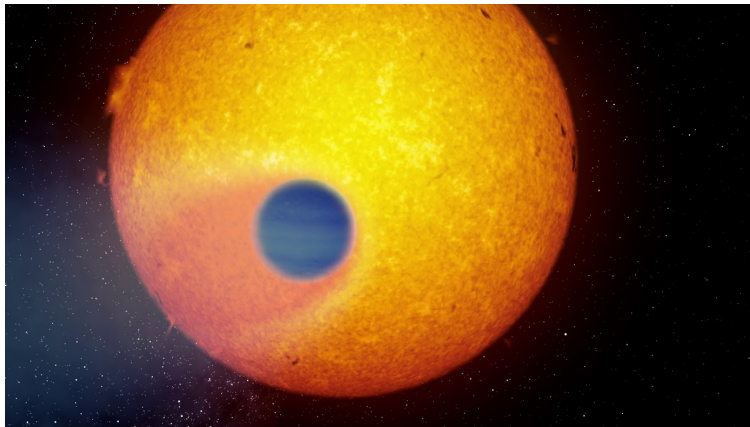
Figure 22: Illustration of the exoplanet WASP-69b. Extracted from IAC Outreach, composition done by Gabriel Pérez Díaz, SMM (IAC).

Hot gas giant exoplanets like WASP-69b can lose part of their atmosphere due to strong stellar irradiation, affecting their physical and chemical evolution. This has been observed by Nortmann et al. (2018), who detected the Helium triplet at 1083 nm in the atmosphere of this planet during the transit as we can see in Figure 23. In this study they also measure the RM effect obtaining a spin orbit angle of $\lambda = 1.2° \pm 1.9°$, extracted from CARMENES spectrograph. We note that the data used in Nortmann et al. (2018) for the RM measurement is the same data used in this project.

The atmosphere of WASP-69b has been previously studied as this exoplanet is an excellent target for atmospheric studies by transmission spectroscopy, due to its large atmospheric scale height (650km) and high planet-to-star ratio, facilitating the detection of a 5.8% excess absorption in the Na D doublet and making the RM's amplitude bigger. This can bee seen in Casasayas-Baris et al. (2017) which used data from HARPS-N and obtained a spin orbit angle of $\lambda = 0.4° \pm 1.9°$.
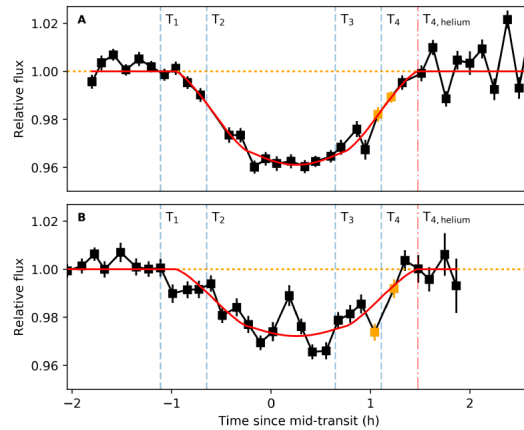
Figure 23: Fitted light curve models used to see that the Helium absorption begins shortly after the planet ingress, with no observable pre-transit absorption. Extracted from the article Nortmann et al. (2018).

Low-mass stars (F-, G-, K- and M-type) stars have a convective layer that, in combination with stellar rotation, produces phenomena associated with magnetic activity. In general, activity in the chromosphere is detected in spectral features such as the activity indicator Ca II, H and K doublet lines at 393.4 and 396.8 nm. WASP-69b is an exoplanet orbiting an active star. For this reason we have to be careful with the RV values, which could be strongly affected by this high activity. In Figure 24 we show one indicator of high activity which is the strong emission in the Ca H & K lines on WASP-69b.
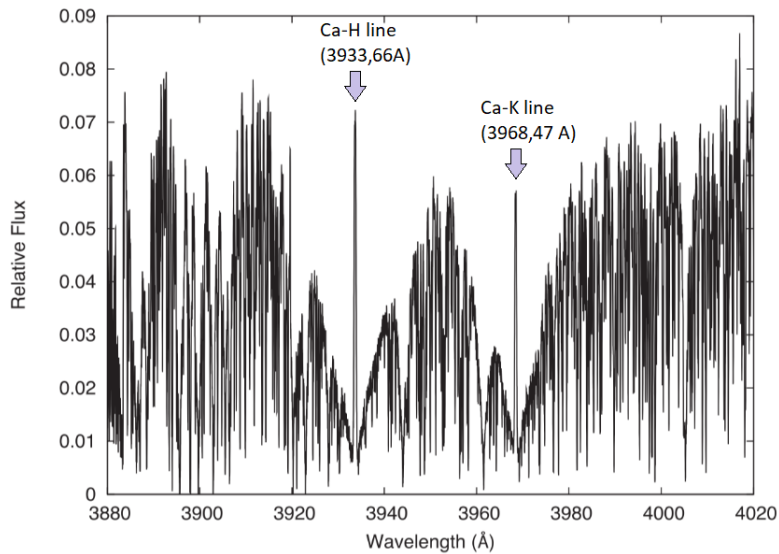

Figure 24: CORALIE spectrum of WASP-69, the marked lines are the Ca II H+K lines. Extracted from the article Anderson et al. (2014).

4 Observations

4.1 CARMENES spectrograph

In recent years, high-resolution spectroscopy has become a frequently-used tool for investigating exoplanet atmospheres. Numerous stable high-resolution spectrographs have been deployed on telescope specifically for exoplanetary science, one of them is the CARMENES spectrograph.

CARMENES (Calar Alto high-Resolution search for M dwarfs with Exoearths with Near-infrared and optical Échelle Spectrographs) is a next-generation instrument built for the 3.5m telescope at the Calar Alto Observatory (the Figure 25) by a consortium of German and Spanish institutions. It has been operational since January 2016 and it consists of two cross-dispersed Echelle spectrographs covering the wavelength ranges from 0.52 to 0.96 μm (visible wavelength range) and from 0.96 to 1.71 μm (near-infrared range) with spectral resolutions R = 80 000-100 000, each of which performs high-accuracy radial-velocity measurements ($\sim$1 m s^{-1}) with long-term stability.
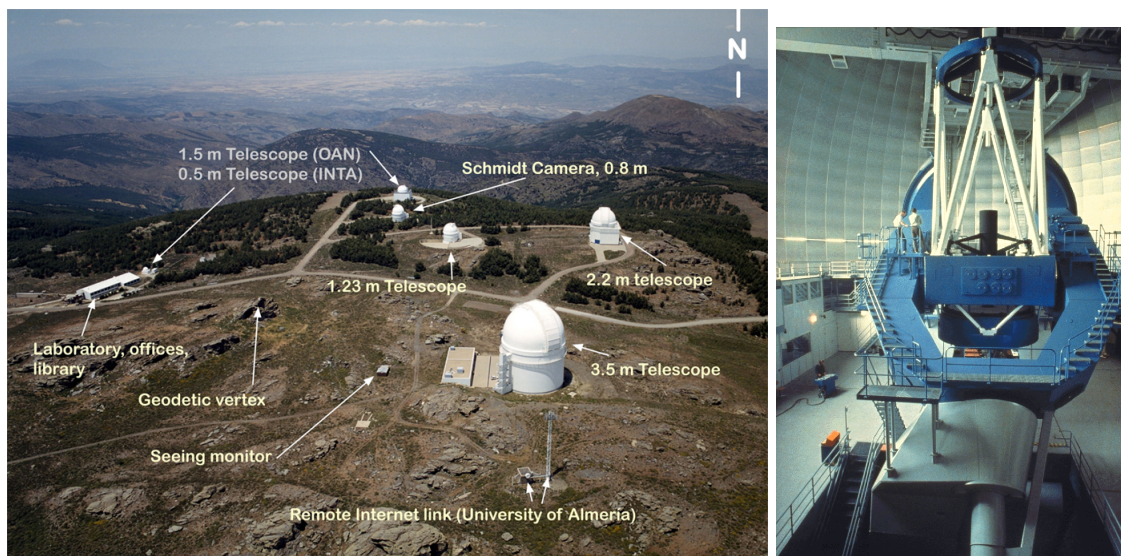

Figure 25: Left: Instalations of the Calar Alto Observatory located in the Sierra de Los Filabres, Almería (Spain). Extracted from Junta de Andalucia's webside. Right: 3.5m telescope where is located CARMENES instrument. Extracted from CAHA webside (*https://www.caha.es/es/*).

CARMENES uses the RV technique, searching for tiny stars oscillations generated by the attraction of the planets surrounding them. One of the main goals of CARMENES is to look for exoearth around M dwarfs. The specific interest of transit surveys focused on M dwarfs (ultracool dwarfs) is that, because of their small radii, signals form an Earth-size planet should be readily distinguishable, although their intrinsic variability may be a limiting factor. Additionally, their habitable zone lies much closer to the host star, thus improving their geometric transit probability. Observations with HARPS further indicate 40% of red dwarfs have a super-Earth class planet orbiting in the habitable zone where liquid water can exist on the surface

This instrument of the Figure 26 has been built specifically for the purpose of obtaining precise RV measurements of cool low-mass stars. The front end of CARMENES is attached to the Cassegrain focus of the Calar Alto 3.5m telescope. Here the light is separated into the visible and near-IR channels

by a dichroic beam splitter centred at 0.96 μm. The two spectral ranges are coupled with fibers into two separated spectrographs, which are mounted on optical banches inside vacuum tanks, which are located in the former coudé laboratory of the 3.5m dome. In our study we will only consider the visible spectrograph (VIS).
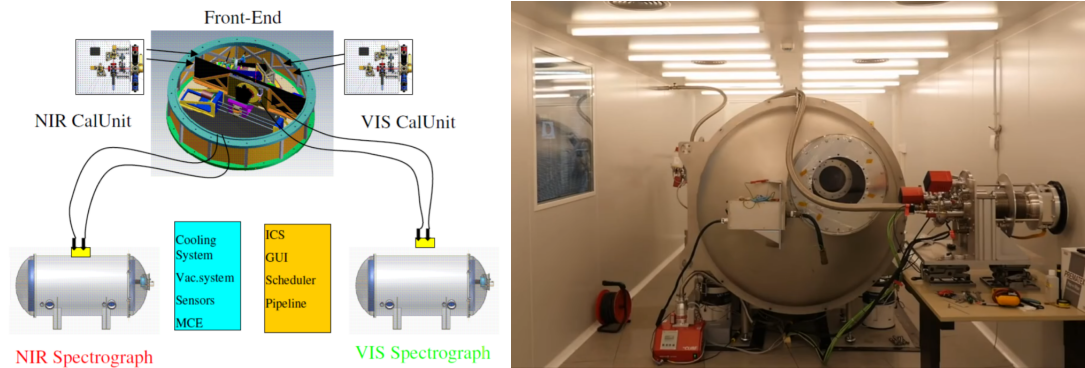

Figure 26: Left: Sketch of the disposition of CARMENES spectrographs. Extracted from the Europen Southern Observatory (ESO) web page. Right: Real image of CARMENES's structure. Extracted from CARMENES webside (*https://carmenes.caha.es/*).

CARMENES is currently used during most nights for the dedicated M star survey, but the instrument is also under heavy demand in "open time" for other scientific topics. The demand for observing time with RV instruments on 4m telescope is expected to rise sharply when the first data from the TESS mission, which objective is to find planets transiting relatively bright stars of all spectral types.

4.2 WASP-69b observations

We used the CARMENES spectrograph to observe two transits of WASP-69b on 2017 August 22 and 2017 September 22 (night 1 and night 2 respectively). The observation spanned approximately four hours for each epoch, which covers the full transit and provides a before- and after-transit baseline. The observation is continuous and the exposition is 292 seconds the first night, and 362 seconds the second one. In total 66 spectra were taken, 31 of them out-of-transit. Both the visible light (VIS) and near infrared (NIR) channels of the instrument were taking exposures quasi-simultaneously. As stated above, we will just use the data from VIS spectrograh. The quality of the spectra is determined, fundamentally, by the seeing, the airmass and the signal-to-noise ratio. The seeing is the quality of the astronomical observations and it depends on the atmospheric conditions of a given night that perturbs the image. The seeing values of the observing nights are shown on Figure 27.

The airmass is the optical path length through Earth's atmosphere for light from a celestial source. As it passes through the atmosphere, light is attenuated by scattering and absorption; the more atmosphere through which it passes, the greater the attenuation. Consequently, celestial bodies at the horizon appear less bright than when at the zenith. So as expected, the observation started at low airmass of 1.97 in both nights.
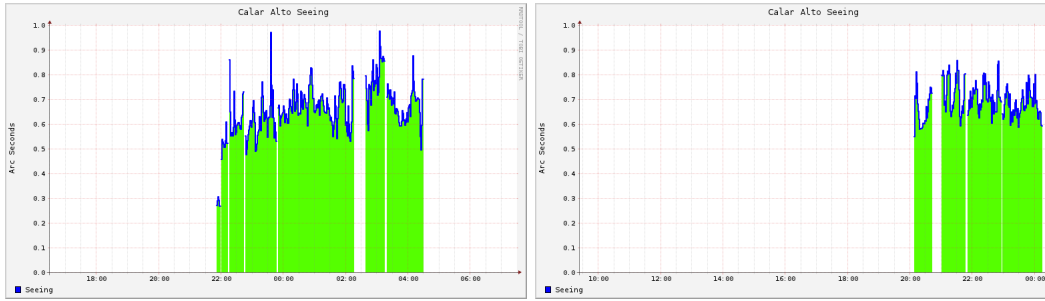
Figure 27: Figures extracted from the historic seeing of the CAHA. Left: 22/08/2017 (night 1). Right: 22/09/2017 (night 2).

The signal-to-noise ratio (SNR) is particular for each transiting stars, each instrument. Exposure time and meteorologic conditions are necessary for the survey to produce a SNR sufficient to peak out the transits and the RM effect with a reasonable confidence.

$$SNR = \frac{signal}{noise} = \frac{mean}{\sigma} \tag{12}$$

In our case the signal is really weak because the star (or our target) has an apparent magnitude of V=9.87 and because we are working with a high resolution spectrograph so the signal needs to be split in a lot of pixels. In the Figure 28 we can see the signal-to-noise ratio obtained in both observing nights, per exposure and per order (colors).
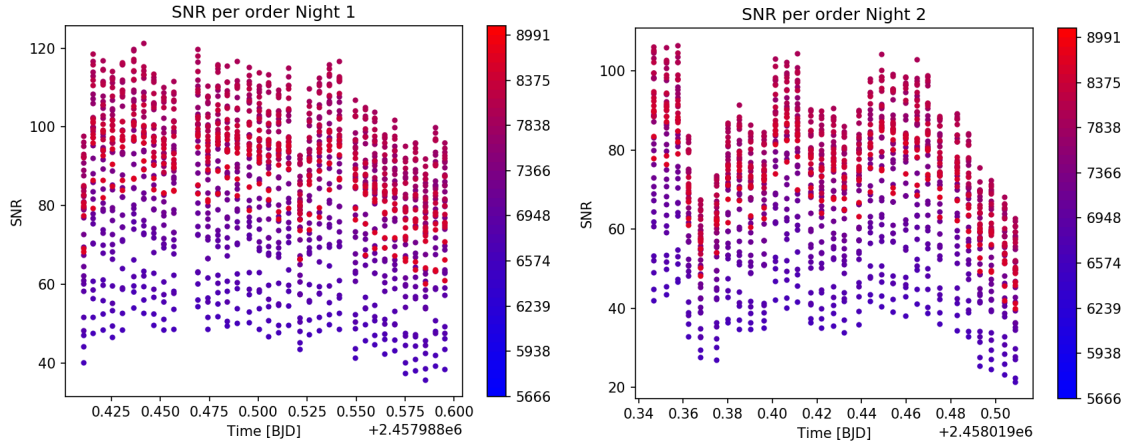
Figure 28: Figures plotted with the Python code. Left: 22/08/2017 (night 1). Right: 22/09/2017 (night 2).

One of the major difficulties of ground-based observations is dealing with the telluric imprints from the Earth's atmosphere. The variation in the transmission of the Earth's atmosphere is one of the main problems when a model is used to correct telluric contaminations: since the telluric transmission during a night depends on the airmass and on water column variations in the air, the atmospheric constituents contaminate the record spectra by producing a time-variable diversity of absorption and emission lines. The main contributors in the optical range are water and molecular oxygen, nevertheless, telluric

sodium signatures near the Na I doublet are also expected. This telluric sodium suffers seasonal variations and, within a night, its behavior is different from the other telluric features, making it necessary to remove these two different contamination sources using different processes. These telluric signatures present a strong dependence on airmass, being more intense at higher airmass and rapidly disapearing at lower airmass. In addition to removing telluric sodium it is necessary to remove the telluric imprints produced by water vapor, the main contributor to the telluric contamination near the Na I doublet.

5 Analysis-Tools

Before explaining the methodology we consider that it is important to explain the tools used in this analysis. Tools for the modelling or analysis of data play an important role in exoplanet research. In this chapter, we give an overview over such tools currently available to the research community.

5.1 SERVAL code

There are many algorithms to compute RVs, which can be grouped depending on their complexity and choices for the model of the reference spectra, number of model parameters, and statistics. These algorithms range from simple cross-correlation with binary masks, to least-squares fit with co-added templates and finally to Gaussian processes. The algorithm choice is influenced by instrument type and the need for accuracy or high precision.

In this work for the computation of the RVs and spectral diagnostics we will use an implemented PYTHON code called SERVAL (SpEctrum Radial Velocity AnaLyser). It is a least-square fitting algorithm and its aim is the highest precision with stabilised spectrographs. The code was developed as the standard RV pipeline for CARMENES. SERVAL (Zechmeister et al. (2018)) uses an iterative approach for the construction of the reference template. The algorithm first derives approximate RVs, measured against an observed spectrum, and then improves the template by co-adding all observed spectra and recomputing the RVs. SERVAL yields not only an output consisting of time series of high precision RVs, but also a number of spectral line indicators that can be useful diagnostic tools for stellar variability. In addition, SERVAL computes indicators of the line width and the wavelength-dependence of the RVs for each observation.

RVs are measured from photospheric absorption lines. Variability of these lines may therefore introduce "noise" on precise RV measurements. The ability to distinguish between such spurious signals and the ones from the planet detection was the main motivation for the dual-spectrograph design of CARMENES, providing access to a large number of activity indicators, and enabling investigations of the observed RV as a function of wavelength. Then the RV is computed separately for each Echelle order, and the slope of the RV vs. $\log \alpha$ determined by a linear fit, yielding the "chromatic index". The chromatic index is a powerful tool to distinguish between RV signals caused by planets and activity-induced signal: the motion of a star around the center of mass of the planetary system is strictly achromatic (i.e., chromatic index = 0 within the measurement errors), whereas the signature of activity is usually stronger at shorter wavelengths, giving rise to non-zero chromatic indices. The pipeline also routinely produces line indices of activity indicators such as Hα, the Na i D lines, and the Ca$_{II}$ infrared triplet for each observation.

5.2 Reflex motion and RM models

We used the model described by Ohta et al. (2005) to simulate the RM effect. This model has already been implemented and can be easily used with the *RmcL* routine of the PyAstronomy library. The RM anomaly of the RV is the first and the main component of the velocity that we will study. It has been previously explained but, briefly, it is a variation of the RV happening over the Doppler reflex motion that an orbiting planet imparts on the rotating host star.

Furthermore, we know that, during the transit, the RVs do not only have the RM effect, but also the contribution of the reflex motion of the star with respect to its own barycentre. The reflex motion has a sinusoidal shape for circular orbits and it is modeled with the routine *SinRadVel* which is also from PyAstronomy library.

The reflex motion is the RV which moves the star due to the presence of a body (in our case, one exoplanet) orbiting around it. This causes a movement around the barycentre of the star-planet

system. It can be calculated within the Kepler's laws considering a circular absolute orbit (like in our case, the planet WASP-69b), which is the orbit of the star around the system barycenter and it's given by:

$$P^2 = \frac{4\pi^2}{GM'}a_s^3 \tag{13}$$

where $M' \equiv \frac{M_p^3}{(M_s+M_p)^2}$. Using the definition of RV semi-amplitude introduced in (4) in combination with (1) we can obtain an alternative expression for K which can be written (Torres et al. (2008), equation 1):

$$\frac{M_p \sin i}{M_J} = 4.919 \times 10^{-3} \left(\frac{K}{\text{kms}^{-1}}\right)\left(1 - e^2\right)^{1/2}\left(\frac{P}{\text{days}}\right)^{1/3}\left(\frac{M_s + M_p}{M_\odot}\right)^{2/3} \tag{14}$$

For a circular orbit with $M_p \ll M_s$ the stellar velocity variations are sinusoidal with amplitude:

$$K = 28.4\text{ms}^{-1}\left(\frac{P}{1 \text{ yr}}\right)^{-1/3}\left(\frac{M_p \sin i}{M_J}\right)\left(\frac{M_s}{M_\odot}\right)^{-2/3} \tag{15}$$

The rutine *SinRadVel* uses the same equation as (13).

With these models we are able to compute the curves presented in Figure 29.

We can also add a third component: the systematic velocity. It is represented as an additional offset due to the system star-planet velocity, in our case it corresponds to the velocity which the system is moving away form the Earth. In the Figure 29, is not represented, but its place would be where the null velocity (0 m/s) is located now. In the case that this velocity is not null, the curves would have an overall offset around the systemic velocity value. In conclusion, in our data, we will consider three components of the velocity: the RM anomaly, the Reflex motion and the systematic velocity.
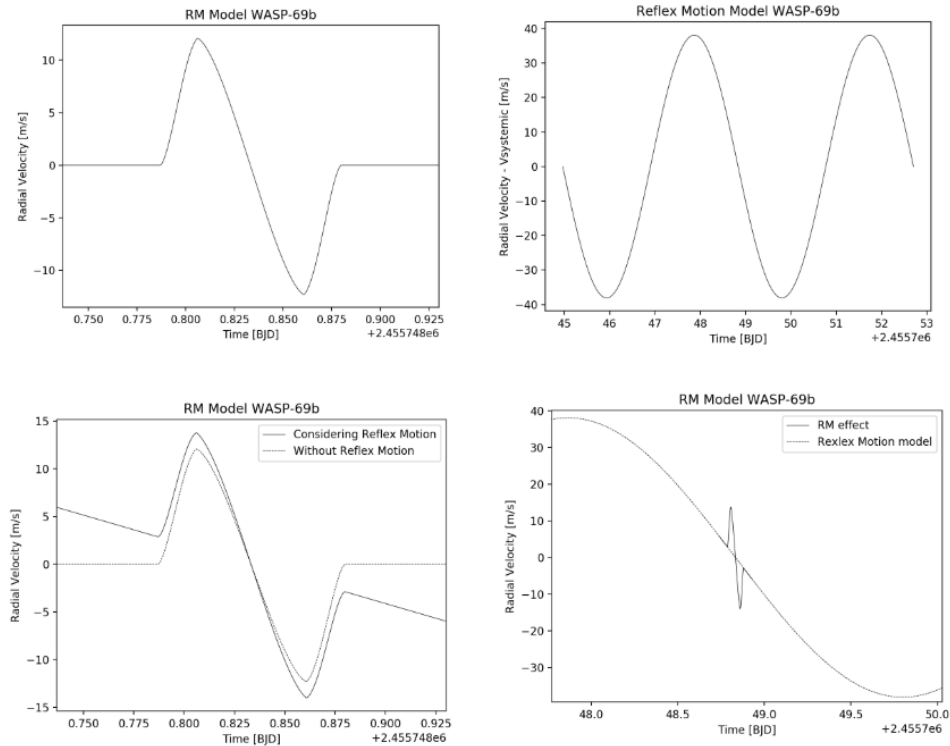
Figure 29: Models calculated using the RmcL and SinRadVel routines from the PyAstronomy library. From top to bottom and from left to right. The figure 1 is the WASP-69b RM model with only this contribution to the RV. The figure 2 is the Reflex motion model of the star, without the RM. The figure 3 is the RM effect with and without considering the reflex motion. The figure 4 is a zoom in the transit zone of the figure 2, but containing the RM effect during the transit.

To study the RM effect we have to introduce some planet parameters like the mass and the radius, some star factors like the effective temperature and the metallicity, and finally some parameters of the system as the orbital period, the semi-major axis and the orbital inclination, among others. But there are some main parameters that affect directly this RM anomaly by changing its behaviour as we can see in Figure 30. These are the following:

- R_p/R_s ratio: it express the quotient between the exoplanet's radius and the host star's radius. We can see that the bigger the difference between radius, the more pronounced the anomaly is. In other words it's less smooth or winding.

- Limb-darkening coefficient: they measure the optical effect in stars, where the limb of the image appears darker than the center part of the disk. In the figure we can see that the central part is the same for all the coefficients, the change is on the sides (ingress and egress) of the anomaly. The change of the RM model is the slightest and it has a sharp-shape.

- Sky-projected spin-orbit angle (λ): it is the angle between the planet's orbit and the star's rotation. It is a very important parameter because it has a lot of uses, like probing how planetary systems form and evolve. We see that it is the value that most alter the RM effect. The shape

for each value is quite similar and the main change is the symmetry of the effect, so it alters the RVs that the planet occult when crossing the stellar disk.

- Angular rotation (ω): it express how fast the angular position or orientation of an object changes with time. In the figure we can see that the main change is in the sharp or pointed shape similar to the effect observed when varying the R_p/R_s values. In other words, it is the rotation on the star around its rotation axis.
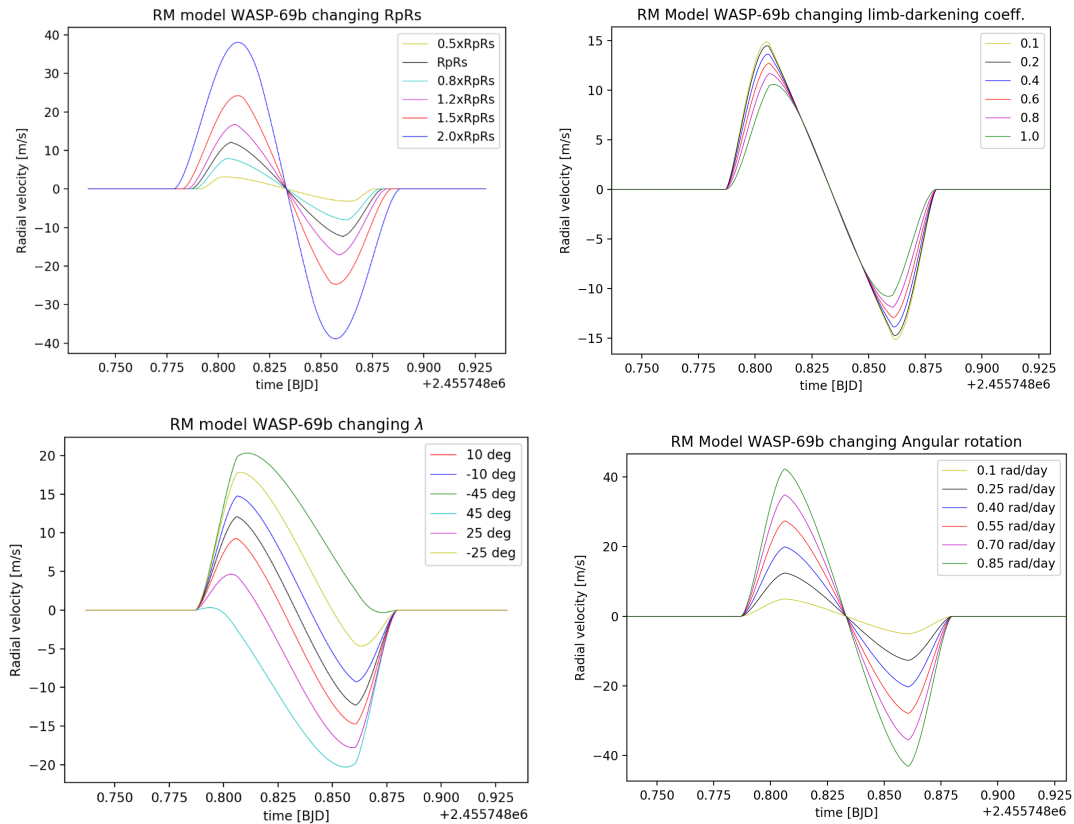
Figure 30: WASP-69b models computed with the RmcL rutines from PyAstronomy library. In all cases, we fix all parameters exept one that varies in a range.

5.3   Fitting procedure

In this section we will explain the general process of fitting a function to empirical data. In this project, we will show several figures displaying best-fitting solutions, we define here how these best-fit results are determined. For the fitting procedure we will use the process of χ^2 minimization along the project. In empirical science, measurements should always be accompanied by estimates of the uncertainty. If a theory predicts a quantity and experimental measures another value its impossible to say whether the experimental has confirmed or falsified the theory without an estimate of the empirical uncertainty. If the empirical measurement was difficult to make the uncertainties should be quite large. Generally, we

assume that experimental results, for instance measurements of a value x, have randomly distributed empirical errors, and consequently have a bell-shaped distribution, described by the Gaussian function:

$$f(x) = \frac{1}{\sqrt{2\pi}\sigma} \exp\left(-\frac{(x-x_0)^2}{2\sigma^2}\right) \tag{16}$$

where x_0 is the mean value obtained for x after a large number of independent measurements, and σ is the uncertainty in a single measurement. Figure 31 shows the shape of this probability distribution.
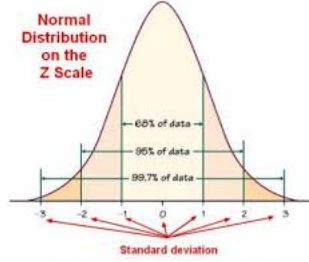
Figure 31: Sketch of the Gaussian or normal distribution. Extracted from *https://gerardnico.com*.

Usually, quantities vary continuously as a function of time, for example the RV measurements. In this case is impossible to make repeated measurements of the identical quantity. Instead, the empirical data consist of a time series: a set $\{x_i, \sigma_i, t_i\}$ of individual measurements (x_i), estimated uncertainty on each measurement (σ_i) and the time of measurement (t_i), and to this time series we will fit a function or model. The choice of model is motivated by an understanding of the orbital motion and relates the planetary system to the reflex RV of the host star. For any set of assumed parameters, we can use the model to calculate predicted values, μ_i, to compare with the measurements $x_i \pm \sigma_i$.

The appropriate way to gauge the goodness of the fit of the model with a particular set of parameters is to calculate a statistical quantity called χ^2 given by

$$\chi^2 = \sum_i \left(\frac{x_i - \mu_i}{\sigma_i}\right)^2 \tag{17}$$

Here the sum is over all the measurements in the set of data. If a particular measurement has a large uncertainty estimate, then the denominator is large, and the contribution to χ^2 is relatively small, even if the deviation between the measured value, x_i, and the corresponding model prediction, μ_i, is large. Because the quantity $x_i - \mu_i$ is squared, positive and negative deviations make equally weighted positive contributions to χ^2. If a model agrees well with the data, the deviation should be small, and consequently the best-fitting model is one with the minimum value of χ^2.

In this project, to apply the fitting procedure, we use the *curve_fit* routine implemented in the SciPy library of Python, which uses non-linear least squares to fit a function to data. We introduce a model function that must take the independent variable as the first argument the parameters to fit as separate remaining arguments, the independent, and the dependent data. The routine returns the optimal values for the parameters so that the sum of the squared error of the function less the dependent data is optimized.

6   Methodology

Here, we present the method and analysis performed in this work. The steps followed to obtain the results are carefully described in this section.

In a very general way, we first look at the observed spectra to see which orders present telluric contamination (from Earth's atmosphere). We then select three samples of data: with all spectra, without strongly telluric contaminated orders and with all telluric contamination corrected. We extract with SERVAL the RVs of these three samples to compare the results. With a Python Notebook (Jupyter Notebook) we compute the RM fitting to extract the parameters of the white and colour light curves.

6.1   Extraction of radial-velocity values with SERVAL code

The first step, in order to improve the results, is to dismiss the most contaminated orders with the purpose to have cleaner spectra. We compare the observed spectra with other spectra without telluric contamination, so we can discard the strongly contaminated orders (or those without stellar information). We note that the spectra without telluric contamination are exactly the same as the contaminated sample, but corrected using an open source ESO tool called *Molecfit*, built for this purpose. This tool removes the Earth's absorption lines from each spectrum in the full range covered by CARMENES. This part of the process is already done by external collaborators before starting the project.

The spectrum's comparison is performed order by order, over a total of 61 orders. In the Figure 32 we can see one telluric contaminated order (right figure) and one non contaminated (left figure). The black spectrum is the telluric corrected spectrum (using Molecfit) and the red is the observed one (including contamination). In the contaminated one, the one spectra differ from each other, while in the non-contaminated the two spectra are almost the same. It is easy to see the similarity along the spectra and conclude if it is highly contaminated or not.
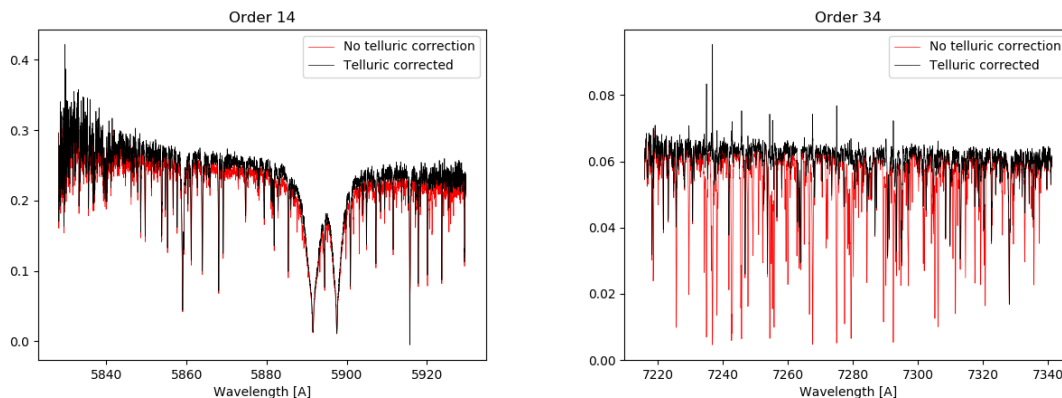
Figure 32: In red we show the observed spectra and in black the telluric corrected spectra. Left: no-contaminated spectrum. Right: contaminated spectrum.

We observed one by one the orders and then we remove the highly contaminated ones. In total, we dismiss 11 orders out of 60, most of them concentrated between the wavelength range of 6820-7420 Å, in the Table 2 we can see the classification of each order.

Order	Wavelength (Å)	State
1-28	5200-6840	No contaminated
29-30	6820-7000	Contaminated
31-32	6980-7160	No contaminated
33-35	7140-7420	Contaminated
36-37	7400-7600	No contaminated
38-39	7580-7800	Contaminated
40-42	7780-8120	No contaminated
43-44	8080-8340	Contaminated
45-49	8300-8940	No contaminated
50-51	8920-9200	Contaminated
52-60	9180-10625	No contaminated

Table 2: Summary of the contaminated and no contaminated ranges.

In our study we will consider three samples with the aim to observe that different extractions with SERVAL pipeline will give us distinct results. The first sample of data is considering the whole spectra (all orders). In the second sample we exclude the highly contaminated orders, so we just considered the orders classified as no contaminated from the Table 2. The last sample is also excluding the highly contaminated orders, and also including an additional correction to the Earth's atmosphere contamination that can remain in the orders that have been selected as "no contaminated" ones. We will refer to this last sample as the name TAC (telluric atmosphere corrected) along this memory.

With SERVAL we extracted the RVs for each sample. We just considered 42 orders out of 61. That is because at the beginning and at the end of the CCD, the signal is too low for SERVAL to extract RV information. In Figure 33 we can see the RVs extracted for each sample during the two observating nights.
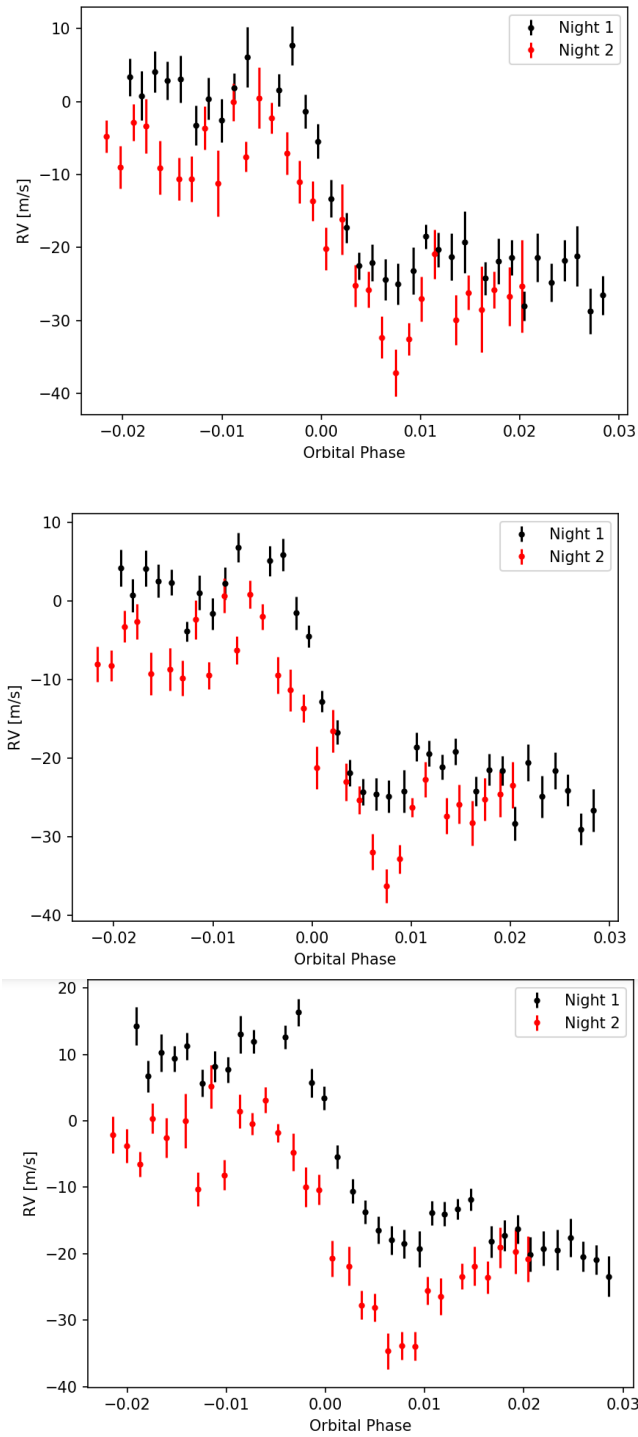
Figure 33: RVs extracted from SERVAL for each sample. We observe the RM effect (white light curve). From top to bottom: all orders, with highly contaminated orders excluded and TAC. In black we show the first night of observation and in red, the second.

6.2 White RM curve fitting

In this section we explain the process followed to obtain the RM's parameters of the white curves:

1. Detrending the RV curve: first we sort the data in time and we then apply a linear regression to the out-of-transit points. With this we are able to fit the reflex motion observed in the out-of-transit data and remove this contribution. After this correction we only have the RM contribution in the RV values. In the Figure 34 we can see an example of one of the samples with the observed white curve and the reflex motion slopes for each night.
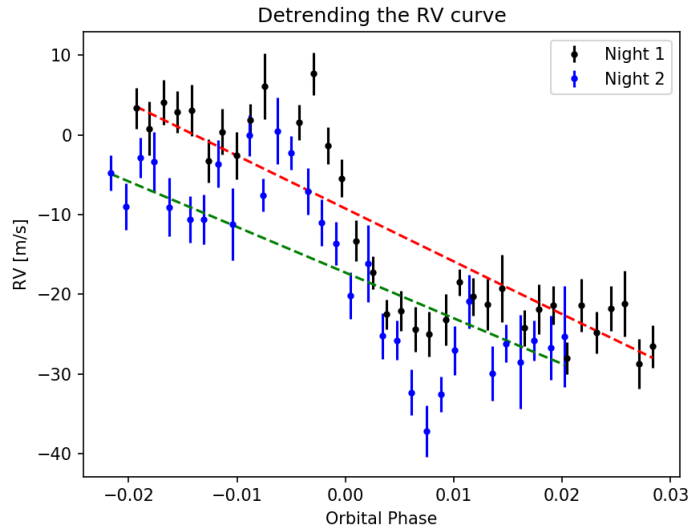
Figure 34: RM effect of two nights (black and blue dots) before detrending. The dashed lines show the reflex motion.

2. Combining data from two nights: in order to have one white curve to analyze we add both nights in a single curve, but we have to keep in mind that we need to change the time scale (x-axis) to a common scale, as we can see in the Figure 35. Our data are given with Barycentric Julian Date (BJD) that is a measure of time that comes from the Julian Date (JD) corrected for differences in the Earth's position with respect to the barycentre of the Solar System. Due to the finite speed of light, the time an astronomical event is observed depends on the changing position of the observer in the Solar System. Before multiple observations can be combined, they must be reduced to a common, fixed, reference time location. To make easier the combination of the spectra of the two nights we convert the time scale to orbital phase. The orbital phase considers the zero position in the center/middle of the host star. When the exoplanet is on the left side of the center we consider a negative phase, the phase will get bigger as far from the center it will be, and positive if it's on the right side.

3. RM fitting: the fitting is done with the RM models presented in section "Analysis-Tools". The RM models depend on 8 parameters: the spin-orbit angle (λ), linear limb-darkening coefficient, R_p/R_s, the time of the transit center (also called epoch), the semimajor axis (a), the orbital inclination (i), the orbital period (P) and the angular rotation (ω). We fix i, a and P to

the literature values observed in Table 22. We leave free the remaining parameters (λ, limb-darkening, R_p/R_s, ω, epoch). In the Figure 35 we see that the RM best fit model agrees on the data.
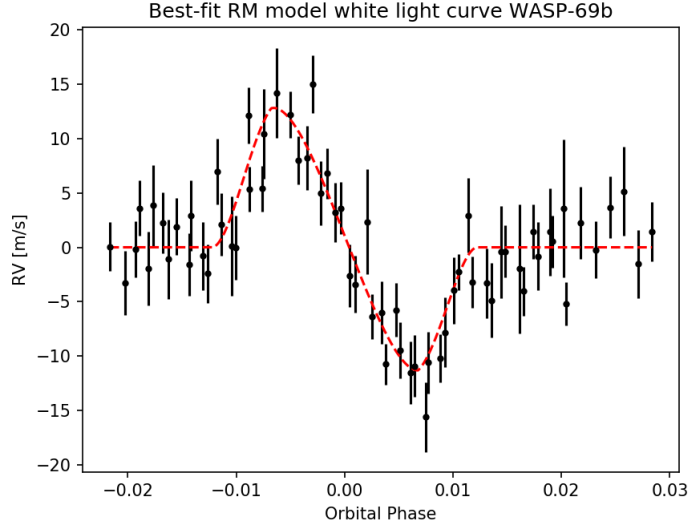

Figure 35: White curve for both nights together, after correcting for the reflex motion (black dots). In red we show the best fit model of the RM effect.

6.3   Colors RM curves fitting

For the fitting of the colors RM curves we reproduced the method used in DiGloria et at.(2015). This method is based on the following steps:

1. Colour RM curves: to extract the colors RV curves we follow the same steps as in section 6.2. from 1 to 2 but for each order. In the Figure 36 we can see the RVs per orders considering both nights together and after detrending.

2. Common mode errors removal: the common mode errors are identical across all orders because they are due of residual instrumental effects, star spots (to first order), stellar differential rotation, or other systematic effects. They can be removed from the data without harm and to do it we consider the RM best fit obtained and we subtract it from the colour RVs. In the Figure 37, for better visualisation, we show the white RM curve with and without the common errors (but we note that this correction is applied to the colour RV curves).

3. Binning in 500 nm passbands: in order to increase the signal we bin the orders in seven passbands of 500 nm wide each one. With the binning we can reduce the errors and consequently get bigger the S/N ratio. To do the binning we did an average of the values corresponding to a range of orders. For each sample the wavelengths range (passband) will be a little different because of the orders considered and excluded. The Figure 38 is one example of the spectrum with the binning in passbands, we can see that the errors have been reduced from the observed RM colors curves represented in the Figure 36.
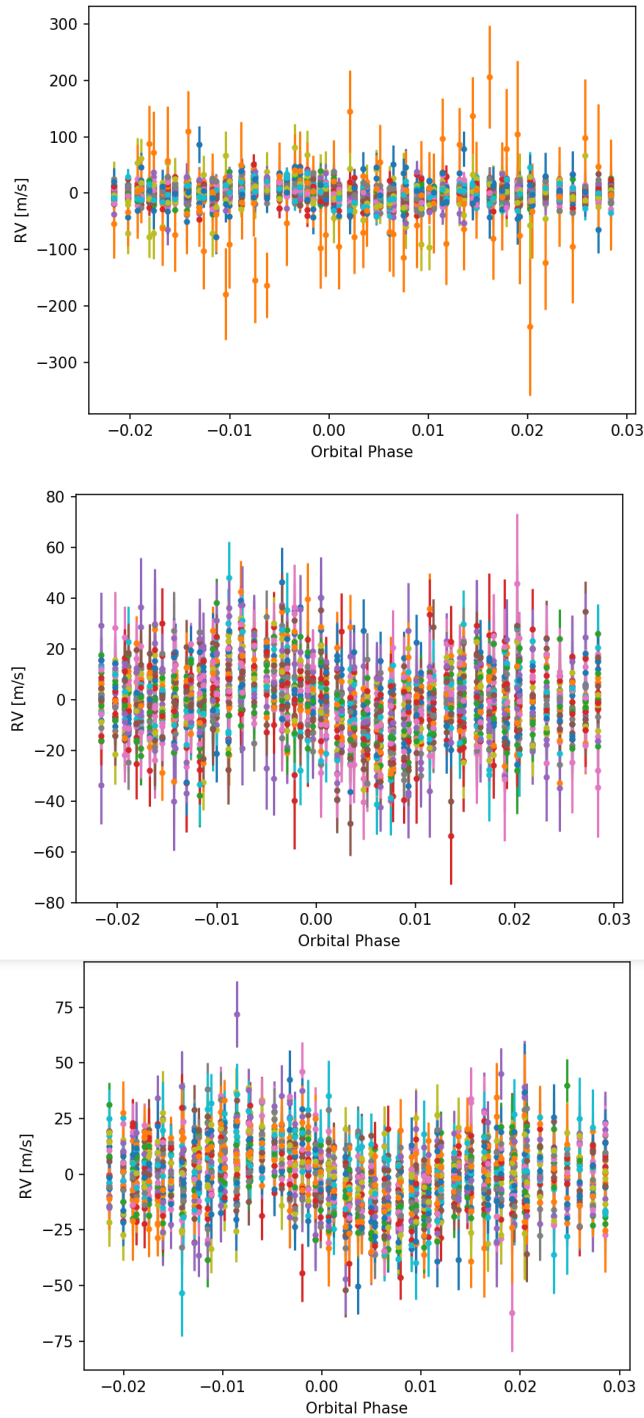
Figure 36: Results of the RVs per order for each sample. Each colour corresponds to one order. From top to bottom: figure 1 is considering all orders, the figure 2 is excluding contaminated orders and the figure 3 is from the TAC sample.
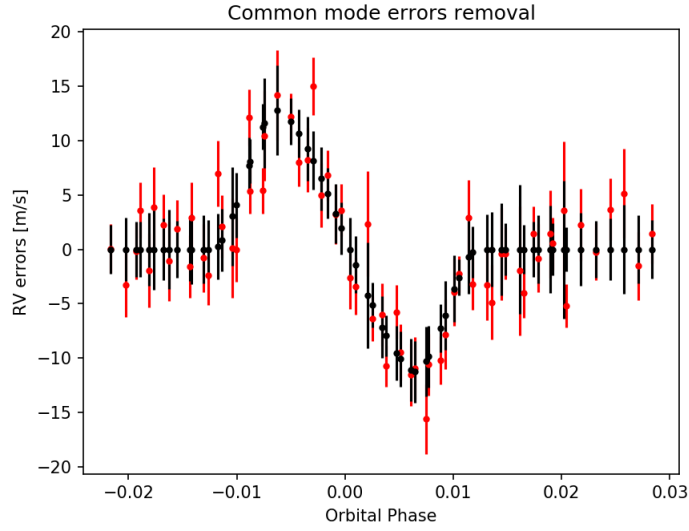
Figure 37: White curve with the common errors and when the common errors are removed. The red curve correspond to observed curve and black curve is the curve dismissing the common errors.
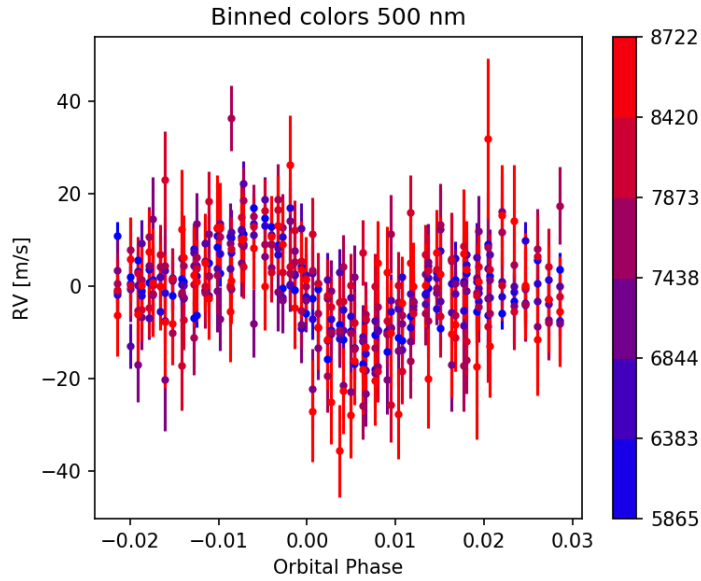
Figure 38: Colour light curves after binning the orders every 500 nm.

4. Colors RM fitting: we fit the RV curves per each wavelength bin fixing the orbital parameters and the limb darkening to the values obtained in the white light curve fitting, and only varying the radius of the planet (R_p/R_s). The amplitude depends on the effective radius of the planet, and since this is wavelength dependent, subsequently the amplitude of the RM effect is also wavelength dependent and can be measured. We are interested in the dependence of the RM

effect on the planet effective size, and the relative change of the R_p/R_s is a function of wavelength, not an absolute value. For each fit we find a R_p/R_s value, so we can then analyze how it change with the wavelength.

To select the limb darkening coefficients we have to consider one different value for each passbands because this parameter is wavelength dependent. We fix this parameter because, as observed in Figure 30, it can influence the final R_p/R_s values. We select the limb-darkening coefficient values for each passband by using a Python toolkit called `PyLDTK`. This toolkit is described in Parviainen, H. Aigrain, S. et al. (2015) and Husser, T. O. et al. (2013) and estimates these values given different wavelength regions. The values used in this work are presented in Table 3.

Passband (nm)	Limb darkening
5615 - 6115	0.75219618
6115 - 6615	0.70184431
6615 - 7115	0.66112630
7115 - 7615	0.60820313
7615 - 8115	0.57897786
8115 - 8615	0.53958984
8615 - 9115	0.52685547

Table 3: Passbands used when binning the data every 500 nm with their respective limb-darkening coefficient.

7 Results

In this section we have measured the RM white curve to get the orbital parameters and the chromatic RM. The chromatic RM effect can give us information about the Rayleigh scattering slope in the transmission spectrum of WASP-69b. This would show that it can be effectively used to measure broadband transmission features, as the RM's amplitude depends on the effective size of the planet, which at the same time depends on the wavelength.
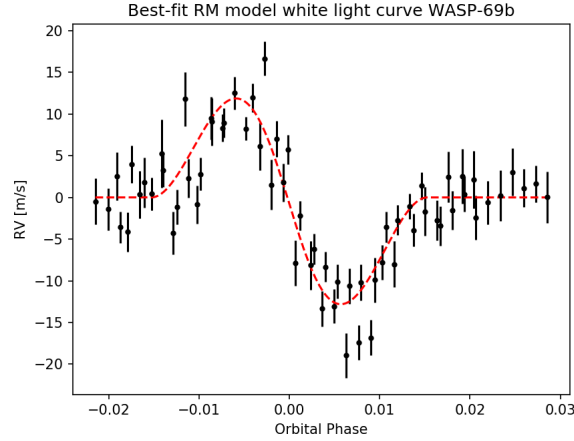
7.1 White curve

The white-light RV time-series with the best fit RM model are presented in Figure 39. These results are obtained after fitting the white curve we get the orbital parameters corresponding to the best-fit model, which are presented in Table 4.

Parameters	All orders	Excluded orders	TAC
λ (deg)	-2.6 ± 1.6	-2.2 ± 1.5	1.4 ± 1.5
Linear limb-darkening	0.96 ± 0.13	0.81 ± 0.14	1.0 ± 0.6
Angular rotation (rad/days)	0.23 ± 0.06	0.15 ± 0.07	0.06 ± 0.04
R_p/R_s	0.15 ± 0.05	0.17 ± 0.04	0.35 ± 0.19

Table 4: Best-fit orbital parameters obtained in the white RM curve fitting. In each column we show the results for one of the studied samples.
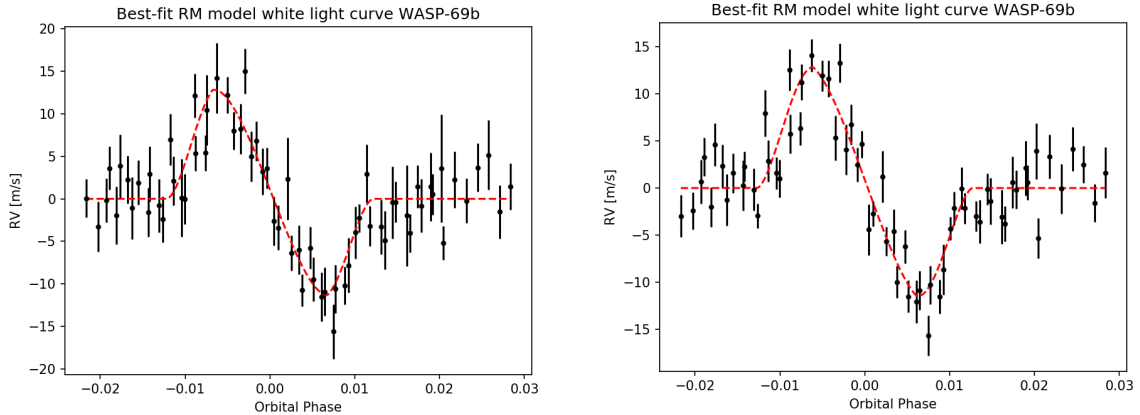
Figure 39: RM white curve data and the best-fit model. From top to bottom: the figure 1 is considering all orders, the figure 2 is excluding contaminated orders and the figure 3 is excluding orders with a telluric contamination correction (TAC). This figure continues in the following page.

Figure 39: Continuation from previous page.

We can first appreciate that the RM RV anomaly is clearly defined in all the extractions. The best fit RM of the white curve changes depending on the sample considered, being the third sample the most smooth one while the others are more sharp-shaped. We can also appreciate significant variation on the errors. The sample where we consider all orders has the biggest errors, meanwhile the samples where we excluded the contaminated orders have smaller errors.

We can see that the best-fit values corresponding to "All orders" and "excluded orders" samples are quite similar, however the data with the TAC correction differ from them. We can compare the obtained parameters with the ones from the literature that also studied WASP-69b such as Casasayas-Barris et al. (2017) and Nortmann et al. (2018) among others. The spin-orbit angle in other studies (Winn et al. (2006), Triaud et al. (2009), Collier Cameron et al. (2010), Cegla et al. (2016)) is retrieved with values ranging from -1.4 ± 1.1 deg to -0.35 ± 0.25 deg. It is a wide range and the values of the wide mask samples are inside the errors. Whereas the values obtained in recent literature are 1.2 ± 1.9 deg (Normann et al. (2018)) and 0.4 ± 1.9 deg (Casasayas-Barris et al. (2017)). All our values will be outside the margin of error in both studies, except the value obtained for excluded orders with TAC correction. The limb darkening coefficient is more similar to both articles, being 0.779 ± 0.048 in Casasayas-Barris et al. (2017) and 0.9 ± 0.1 in Nortmann et al. (2018). We can also compare the angular rotation with the one obtained in Casasayas-Barris et al. (2017) which obtained a value of 0.24 ± 0.02 rad/days and we can observe that the all orders and excluded orders with a wide mask are almost the same. However the TAC value is very different.

7.2   Color curve and Rayleigh scattering

After following the steps described in the methodology we obtain the colors RV curve of the two nights together and the same curve but binning some orders, reducing 42 orders in 7 passbands with a wavelength ranges of 500 nm each. The results obtained are represented in Figure 40.
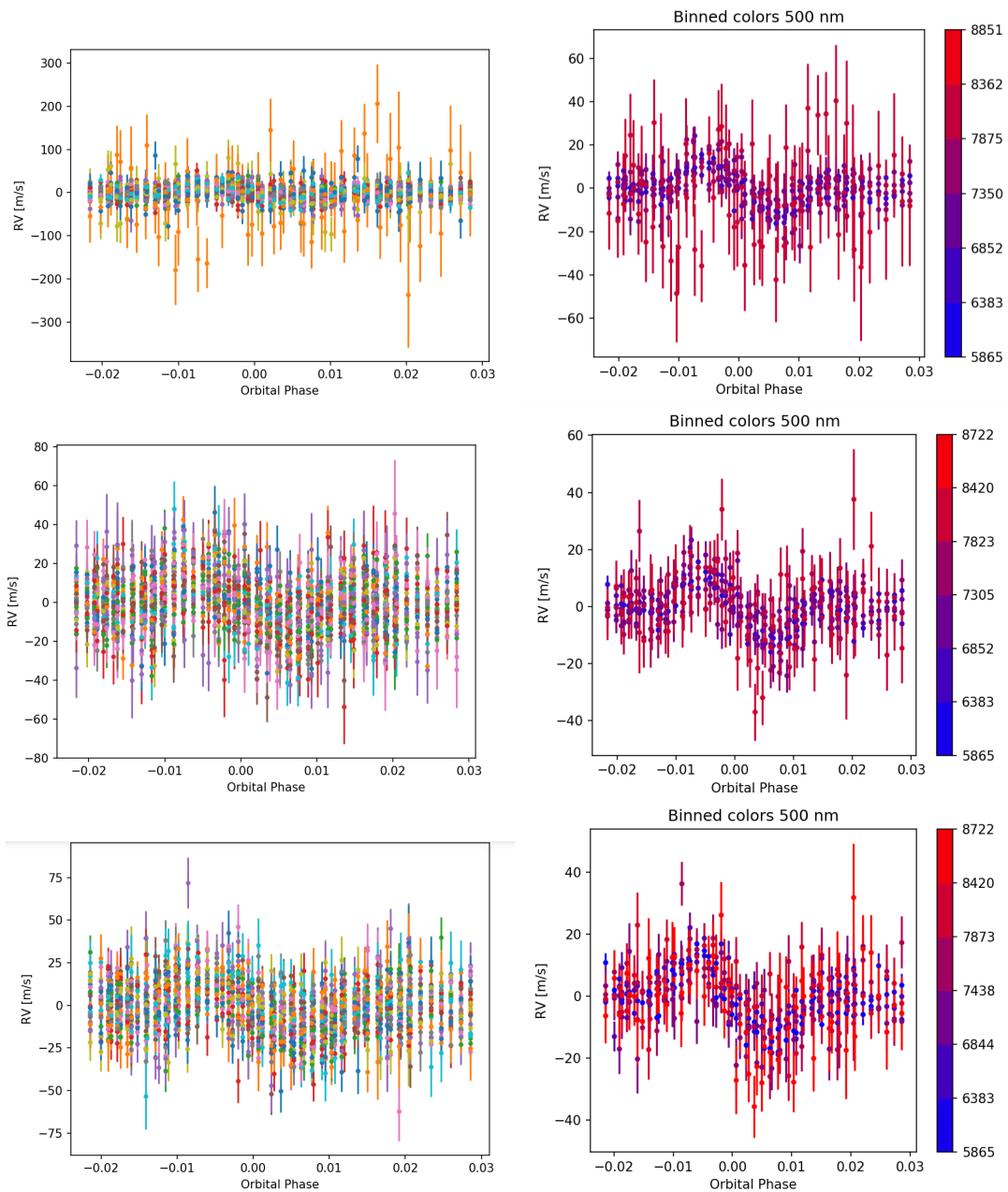
Figure 40: RV curves of each order (left column) and RV curves after binning the orders in 500 nm passbands (right column). The central wavelength of the binned passbands is presented in the colour-bar. From top to bottom: the first row is considering all orders, the second row is excluding contaminated orders and the third row is excluding orders with a telluric contamination correction (TAC).

In the figure we can see again that the errors are larger in the sample that consider all orders,

basically because the orders with a small number of stellar lines have been removed from the sample, and are not shown in the plots. The smallest errors are the ones in the excluded orders with TAC correction which are smaller than the sample where we only exclude orders, meaning telluric lines have influence in the RV extraction.

In the observed colors curves (left column) we can observe a lot of dispersion but we can observe that after binning the orders the errors drastically decrease. It is very easy to see this comparison if we pay attention on the y-axis, which is reduced more than one order of magnitude.

In order to obtain the value of the planet effective size for each passband we perform a fit for each band, getting in that way the evolution of the planet radius with the wavelength, also called the Rayleigh scattering slope. In the Figure 41 we can see the resulting planet-star radius ratio as function of wavelength, indicating the error bars.
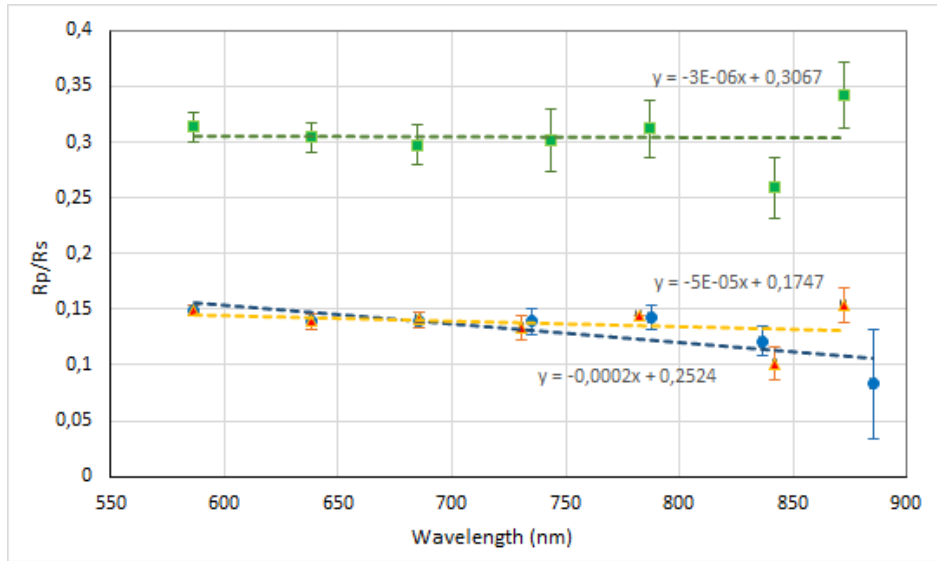
Figure 41: Evolution of the planet size with wavelength. Green dots express the data excluding orders and with TAC correction; blue dots express the data considering all orders; yellow dots express the data excluding orders. The dashed lines are the lineal regressions and their errors.

We expected a negative slope corresponding to the Rayleigh scattering. The result obtained using the sample with excluded orders and TAC corrected has nearly a flat regression and differ a lot from the results obtained with the other samples. Specially because it shows an offset, which is not consistent with the expected R_p/R_s value (comparing with literature). This is also observed in table 4, where the R_p/R_s for the TAC sample is far from the literature value. On the other hand, the other two samples present consistent results and linear regressions. The fit has a slope of: -0.00016 ± 0.01542 for all orders, 0.00005 ± 0.01785 for excluded orders and 0.000003 ± 0.027031 for excluded orders with telluric correction (TAC). With the values of the gradient we can see that the lines have a very small inclination and very large errors.

If we compare the samples without telluric correction, we can see that the error is smaller when we exclude the contaminated orders. We can notice that the errors are bigger in the lasts orders, especially when we consider all orders, and it can be explained because, as we have seen in the previous sections, the higher orders are more contaminated.

8   Conclusions and discussion

In this project we have first studied the exoplanets detection methods in general, specially those necessary for the project: the transits and RVs. After that, we focused on the RM effect, and observed how it depends on the planet-star system parameters.

Then, we studied, for three different cases, how the RV extraction affects to the measured RM parameters. In general, after the analysis of different extractions, we have noticed that the results are different, so the final results strongly depend on the extraction. We have seen that telluric contaminated orders or orders without stellar information induce noise in the final RV curves. So the first conclusion is that different extractions with SERVAL pipeline gives us different results.

The white curve results are the expected, because the RM effect is clearly defined, and the errors decrease visibly when we exclude the contaminated orders. If we compare the samples with excluded orders we see that the difference between the errors is not so obvious. In the results, some of the orbital parameters obtained from the best fit models are quite similar like the limb darkening coefficient and the angular rotation. However, the spin-orbit angle remains out of the margin of error considered in Casasayas-Barris et al. (2017) and Nortmann et al. (2018). Although we use the same data as Nortmann et al. (2018), the result are not consistent.

The second objective of our study was try to measure the chromatic effect following the method introduced by DiGloria et al. (2015). It is the first time that the RM chromatic is performed for our exoplanet, WASP-69b. The obtained evolution of the planet radius from the colors curve is completely different from the DiGloria et al. (2015) result. We note, however, that they use data from a different planet and instrument. In the other hand, comparing with the same literature, our slope is less evident (with less inclination) and with higher errors. We obtained a results with a lot of error that makes us imposible to claim the Rayleigh scattering in the atmosphere of WASP-69b. This is basically due to the S/N of the observed spectra, as the star is relatively faint for this kind of studies. However, it's probably a good candidate to observe with spectrographs located in larger telescopes, like the new generation Echelle spectrograph ESPRESSO placed in the VLT with 8m telescopes. It's not possible to observe it with the current ESPRESSO because it's located on the south hemisphere and our target it's only visible from the north.

Additionally, for further studies with CARMENES, we could analyze the spectral line indicators as stellar variability diagnostic tools. In particular, chromatic RM studies, which need high precision, require more accurate analysis of the stellar variability than those presented here. For example, by taking advantage of the chromatic index and other activity indicators (Na I, Hα,...). This is particularly important for active stars like WASP-69.

References

[1] A. Johnson and N. W. Joshua. Analytic description of the rossiter-mclaughlin effect for transiting exoplanets: Cross-correlation method and comparison with simulated data. *arXiv preprint arXiv:0910.2365*, 2009.

[2] J. N. Winn. Exoplanet transits and occultations. *Exoplanets*, 1:55–77, 2010.

[3] G. Boué, M. Montalto, I. Boisse, M. Oshagh, and N. Santos. New analytical expressions of the rossiter-mclaughlin effect adapted to different observation techniques. *Astronomy & Astrophysics*, 550:A53, 2013.

[4] D. Sing, J. Fortney, N. Nikolov, H. E. Wakeford, T. Kataria, T. M. Evans, S. Aigrain, G. E. Ballester, A. Burrows, D. Deming, et al. A continuum from clear to cloudy hot-jupiter exoplanets without primordial water depletion. *Nature*, 529(7584):59, 2016.

[5] N. Casasayas-Barris, E. Palle, G. Nowak, F. Yan, L. Nortmann, and F. Murgas. Detection of sodium in the atmosphere of wasp-69b. *Astronomy & Astrophysics*, 608:A135, 2017.

[6] L. Nortmann, E. Pallé, M. Salz, J. Sanz-Forcada, N. Evangelos, F. J. Alonso-Floriano, S. Czesla, F. Yan, G. Chen, I. A. G. Snellen, et al. Ground-based detection of an extended helium atmosphere in the saturn-mass exoplanet wasp-69b. *Science*, 362(6421):1388–1391, 2018.

[7] Y. Ohta, A. Taruya, and Y. Suto. The rossiter-mclaughlin effect and analytic radial velocity curves for transiting extrasolar planetary systems. *The Astrophysical Journal*, 622(2):1118, 2005.

[8] Amaury HMJ Triaud. The rossiter–mclaughlin effect in exoplanet research. *Handbook of Exoplanets*, pages 1375–1401, 2018.

[9] Jason T Wright. Radial velocities as an exoplanet discovery method. *Handbook of Exoplanets*, pages 1–13, 2017.

[10] D.R. Anderson, A. Collier Cameron, L. Delrez, A. P. Doyle, F. Faedi, A. Fumel, M. Gillon, Y. Gómez Maqueo Chew, C. Hellier, E. Jehin, et al. Three newly discovered sub-jupiter-mass planets: Wasp-69b and wasp-84b transit active k dwarfs and wasp-70ab transits the evolved primary of a g4+ k3 binary. *Monthly Notices of the Royal Astronomical Society*, 445(2):1114–1129, 2014.

[11] J. N. Winn. The rossiter-mclaughlin effect for exoplanets. In *EPJ Web of Conferences*, volume 11, page 05002. EDP Sciences, 2011.

[12] A. Quirrenbach, P. J. Amado, I. Ribas, A. Reiners, J. A. Caballero, W. Seifert, J. Aceituno, M. Azzaro, D. Baroch, D. Barrado, et al. Carmenes: high-resolution spectra and precise radial velocities in the red and infrared. In *Ground-based and Airborne Instrumentation for Astronomy VII*, volume 10702, page 107020W. International Society for Optics and Photonics, 2018.

[13] E. Di Gloria, I. A. G. Snellen, and S. Albrecht. Using the chromatic rossiter-mclaughlin effect to probe the broadband signature in the optical transmission spectrum of hd 189733b. *Astronomy & Astrophysics*, 580:A84, 2015.

[14] B. S. Gaudi and J. N. Winn. Prospects for the characterization and confirmation of transiting exoplanets via the rossiter-mclaughlin effect. *The Astrophysical Journal*, 655(1):550, 2007.

[15] F. Faedi, S. Barros, D. Pollacco, E. K. Simpson, J. McCormac, V. Moulds, C. Watson, I. Todd, F. Keenan, A. Fitzsimmons, et al. New transiting exoplanets from the superwasp-north survey. *Proceedings of the International Astronomical Union*, 6(S276):143–147, 2010.

[16] M. Zechmeister, A. Reiners, P. J. Amado, M. Azzaro, F. F. Bauer, V. J. S. Béjar, J. A. Caballero, E. W. Guenther, H. J. Hagen, S. V. Jeffers, et al. Spectrum radial velocity analyser (serval)-high-precision radial velocities and two alternative spectral indicators. *Astronomy & Astrophysics*, 609:A12, 2018.

[17] I. A. G. Snellen. A new method for probing the atmospheres of transiting exoplanets. *Monthly Notices of the Royal Astronomical Society*, 353(1):L1–L6, 09 2004.

[18] R. A. Rossiter. On the detection of an effect of rotation during eclipse in the velocity of the brigher component of beta Lyrae, and on the constancy of velocity of this system. , 60, July 1924.

[19] F. Pont, H. Knutson, R. L. Gilliland, C. Moutou, and D. Charbonneau. Detection of atmospheric haze on an extrasolar planet: the 0.55-1.05 μm transmission spectrum of HD 189733b with the HubbleSpaceTelescope. , 385:109–118, March 2008.

[20] H. Parviainen and S. Aigrain. Ldtk: limb darkening toolkit. *Monthly Notices of the Royal Astronomical Society*, 453(4):3821–3826, 2015.

[21] T-O Husser, S. Wende-von Berg, S. Dreizler, D. Homeier, A. Reiners, T. Barman, and P. H. Hauschildt. A new extensive library of phoenix stellar atmospheres and synthetic spectra. *Astronomy & Astrophysics*, 553:A6, 2013.

[22] A. Odunlade and A. E. Pauline. Transiting exoplanets: characterisation in the presence of stellar activity. 2010.

[23] X. Fu, F. Duan, J. Jiang, T. Huang, L. Ma, and C. Lv. Astigmatism-corrected echelle spectrometer using an off-the-shelf cylindrical lens. *Applied optics*, 56(28):7861–7868, 2017.

[24] W. Becker, M. Kramer, and A. Sesana. Pulsar timing and its application for navigation and gravitational wave detection. *Space Science Reviews*, 214(1):30, 2018.

[25] A. C. Cameron, V. A. Bruce, G. Miller, A. Triaud, and D. Queloz. Line-profile tomography of exoplanet transits–i. the doppler shadow of hd 189733b. *Monthly Notices of the Royal Astronomical Society*, 403(1):151–158, 2010.

[26] F. Pont, D. K. Sing, N. P. Gibson, S. Aigrain, G. Henry, and N. Husnoo. The prevalence of dust on the exoplanet hd 189733b from hubble and spitzer observations. *Monthly Notices of the Royal Astronomical Society*, 432(4):2917–2944, 2013.

[27] P. R. McCullough, N. Crouzet, D. Deming, and N. Madhusudhan. Water vapor in the spectrum of the extrasolar planet hd 189733b. i. the transit. *The Astrophysical Journal*, 791(1):55, 2014.

[28] A. Collier Cameron, D. M. Wilson, R. G. West, L. Hebb, X-B. Wang, S. Aigrain, F. Bouchy, D. J. Christian, W. I. Clarkson, B. Enoch, et al. Efficient identification of exoplanetary transit candidates from superwasp light curves. *Monthly Notices of the Royal Astronomical Society*, 380(3):1230–1244, 2007.

[29] J. N. Winn, J. A. Johnson, G. W. Marcy, R. P. Butler, S. Vogt, G. W. Henry, A. Roussanova, M. J. Holman, K. Enya, N. Narita, et al. Measurement of the spin-orbit alignment in the exoplanetary system hd 189733. *The Astrophysical Journal Letters*, 653(1):L69, 2006.

[30] David Russell. Geophysical classification of planets, dwarf planets, and moons. *arXiv preprint arXiv:1308.0616*, 2013.

[31] A. Triaud, D. Queloz, F. Bouchy, C. Moutou, A. C. Cameron, A. Claret, P. Barge, W. Benz, M. Deleuil, T. Guillot, et al. The rossiter-mclaughlin effect of corot-3b and hd 189733b. *Astronomy & Astrophysics*, 506(1):377–384, 2009.

[32] H. M. Cegla, C. Lovis, V. Bourrier, B. Beeck, C. A. Watson, and F. Pepe. The rossiter-mclaughlin effect reloaded: Probing the 3d spin-orbit geometry, differential stellar rotation, and the spatially-resolved stellar spectrum of star-planet systems. *Astronomy & Astrophysics*, 588:A127, 2016.

[33] M. Perryman. *The exoplanet handbook*. Cambridge University Press, 2018.

[34] H. J. Deeg and J. A. Belmonte. *Handbook of Exoplanets*. Springer, 2018.

[35] C. A. Haswell. *Transiting exoplanets*. Cambridge University Press, 2010.

[36] Rayleigh scattering in exoplanet atmospheres nasa exoplanet exploration. `https://exoplanets.nasa.gov/resources/168/rayleigh-scattering-in-exoplanet-atmospheres/`. Accessed: 2019-08-30.

[37] Lecture Notes 7: Rayleigh scattering princeton university cefrc. `https://cefrc.princeton.edu/sites/cefrc/files/`. Accessed: 2019-08-30.

[38] Rossiter-McLaughlin model class pya group (ohta et al. 2005). `https://pyastronomy.readthedocs.io/en/latest/modelSuiteDoc/RmcLOhtaDoc/rmcl.html`. Accessed: 2019-08-30.

[39] Circular orbit—radial-velocity shift pya group. `https://pyastronomy.readthedocs.io/en/latest/modelSuiteDoc/radVelDoc/radVel.html?highlight=sinusoidal`. Accessed: 2019-08-30.

[40] Planet WASP-69 b exoplanet.eu catalogue. `http://exoplanet.eu/catalog/wasp-69_b/`. Accessed: 2019-08-30.

[41] Centro Astronómico Hispano-Alemán caha. `https://www.caha.es/es/`. Accessed: 2019-08-30.

[42] CARMENES caha. `https://www.caha.es/es/`. Accessed: 2019-08-30.

[43] Exoplanet Exploration nasa. `https://exoplanets.nasa.gov/`. Accessed: 2019-08-30.